

Concentration polarization induced phase rigidification in ultralow salt colloid chemistry to stabilize cryogenic Zn batteries

Received: 2 June 2024

Accepted: 21 October 2024

Published online: 01 November 2024

 Check for updatesBaojiu Hao¹, Jinqiu Zhou¹✉, Hao Yang¹, Changhao Zhu¹, Zhenkang Wang¹, Jie Liu¹, Chenglin Yan^{2,3} & Tao Qian¹✉

The breakthrough in electrolyte technology stands as a pivotal factor driving the battery revolution forward. The colloidal electrolytes, as one of the emerging electrolytes, will arise gushing research interest due to their complex colloidal behaviors and mechanistic actions at different conditions (aqueous/nonaqueous solvents, salt concentrations etc.). Herein, we show “beyond aqueous” colloidal electrolytes with ultralow salt concentration and inherent low freezing points to investigate its underlying mechanistic principles to stabilize cryogenic Zn metal batteries. Impressively, the “seemingly undesired” concentration polarization at the interface would disrupt the coalescence stability of the electrolyte, leading to a mechanically rigid interphase of colloidal particle-rich layer, positively inhibiting side reactions on either side of the electrodes. Importantly, the multi-layered pouch cells with cathode loading of 10 mg cm⁻² exhibit undecayed capacity at various temperatures, and a relatively high capacity of 50 mAh g⁻¹ could be well maintained at -80 °C.

Electrolytes constitute a fundamental and indispensable constituent within the realm of battery chemistry. While they may not directly impact the energy density of batteries, electrolytes, and their associated interfaces exert significant influences on the stability of cathode and anode, cycling life, and power density. Many state-of-the-art electrolytes have been designed, incorporating not only conventional strategies of functional additives¹, high-concentration electrolytes^{2–5}, quasi-solid or solid electrolytes^{6,7}, but also emerging innovative strategies including suspended electrolyte⁸, eutectic electrolyte^{9,10}, nano solid electrolyte¹¹, and colloidal electrolyte (CE)^{12,13}, etc, to modify the ionic solvation structure and improve batteries’ reversibility. Among them, the recently proposed CEs stand out as a promising category of electrolytes. In particular, thanks to the compatibility of colloids in the aqueous and “beyond aqueous” phases, many kinds of CEs have been reported in the field of lithium metal/ion battery and aqueous batteries. For example, trace amount of lithium thiocarbonate colloid¹⁴,

covalent organic nanosheet colloid¹⁵ in commercial carbonate electrolyte can tune the microscopic Li⁺ solvation structure and tailor the interfacial charge transfer. Lithium magnesium silicate¹⁶, palygorskite¹⁷, and graphene oxide quantum dots¹⁸ are introduced into the aqueous solution to improve the reversibility of metal anode plating/stripping behavior and regulate the ice growth at cryogenic environment.

However, it should be noted that the colloid is a complex and dynamic polyphase mixture consisting of dispersing medium, colloid particles, and electric double layer around colloid particles. Given the fluidity of the liquid and the complexity of the composition of the colloidal system, they exhibit complex and changing macroscopic physical properties that do not conform to standard concepts of solids, liquids, or gases¹⁹. Especially for CEs, the presence of dissolved saline ions imparts its unforeseen properties. Unfortunately, it has not been noticed yet to study the colloid chemistry and colloid behavior in

¹School of Chemistry and Chemical Engineering, Nantong University, Nantong, China. ²School of Petrochemical Engineering, Changzhou University, Changzhou, China. ³Key Laboratory of Core Technology of High Specific Energy Battery and Key Materials for Petroleum and Chemical Industry, College of Energy, Soochow University, Suzhou, China. ✉e-mail: jqiu Zhou@ntu.edu.cn; qiantao@ntu.edu.cn

CEs. Although the CEs may appear as a homogeneous solution, it is important to note that there exists a distinct physical interface between the colloidal particles and the medium, rendering it an inherently non-uniform system with ultra-high dispersion and multi-phase characteristics. Stable CEs must possess both coalescence stability and dynamic stability, with a greater emphasis on the former. The mutual repulsion of charges on the surface of colloidal particles is a key determinant for their coalescence stability²⁰. Our team proposed to disrupt the coalescence stability state by highly concentrated salt in order to generate a colloidal quasi-solid electrolyte directly²¹. However, the underlying mechanism governing the behavior of CEs in low-concentration salt conditions remains elusive. It is noteworthy that low-concentration salts exhibit significant potential with a genuine sense of cost-effectiveness^{22–24}. During the battery cycle process, factors such as the electric field effect and its constantly changing direction, ion concentration's variations at the interface, and bulk phase of electrolyte can significantly influence both the stable state and motion behavior of colloidal particles. This particular aspect pertaining to CEs remains inadequately investigated.

Zinc metal batteries (ZMBs) have emerged as a promising candidate for large-scale energy storage owing to their high safety, abundant materials availability, and the inherent advantages of Zn in terms of low redox potential (−0.76 V vs. standard hydrogen electrode) and high theoretical capacity (820 mAh g^{−1})²⁵. However, due to the influence of active water in aqueous electrolytes, a range of issues such as the growth of dendrites, hydrogen evolution reaction, side reactions, and dissolution of cathode severely hinder the further development of ZMBs^{26,27}. The “beyond aqueous” electrolytes, devoid of water, effectively circumvent water decomposition, and the generation of water-related byproducts. In comparison to aqueous electrolytes, these “beyond aqueous” counterparts demonstrate a broad electrochemical stability range and exceptional thermodynamic stability for Zn anodes, resulting in enhanced reversibility of Zn plating/stripping with heightened Coulombic efficiencies²⁸. Furthermore, colloidal particles exhibit compatibility with “beyond aqueous” electrolyte systems, and the majority of “beyond aqueous” solvents exhibit remarkably low freezing points. These advantages confer significant potential to CEs in practical applications of ZMBs under non-standard conditions, such as cold environments, and in terms of industrialization, primarily due to the inherent properties and cost considerations associated with electrolytes^{29–31}.

Based on the above considerations, we elaborately design ultralow-salt-concentration “beyond aqueous” colloid electrolytes (ULCE) to stabilize the ultralow-temperature ZMBs. The unique physiochemistry and colloid behavior of ULCE realize peculiar phase rigidification on the electrolyte and electrode interface. Specifically, the inherent concentration polarization phenomenon occurring during battery cycling results in an elevated zinc ion concentration at the electrode/electrolyte interface on the Zn stripping side³²:

$$C_e = C_o \cdot e^{\eta n F / RT} \quad (1)$$

Where C_e is the solution ion concentration on electrode interface, C_o is the bulk solution ion concentration, and η is the overpotential (positive value).

The elevated C_e would lead to excessive neutralization of surface charge on colloidal particles, thus disrupting their coalescence stability, leading to their destabilization and agglomeration at the electrode/electrolyte interface. Therefore, this “seemingly undesired” side reaction caused by uneven interfacial ion concentration due to concentration polarization can be positively reinforced through a low-concentration salt CE, ultimately in situ generating a mechanically rigid phase of colloidal particle-rich solidified layer on the electrode surface³³. Surprisingly, this solidified layer exhibits exceptional effects on enhancing cycling performance for both anode and cathode. The

solidified layer facilitates rapid desolvation of Zn²⁺ ions and concurrently enhances the interfacial compatibility between the electrode and electrolyte. The continuous and compact protective layer at the interface not only acts as a barrier to shield solvents and dissolved ions, safeguarding Zn metal from electrolyte corrosion, but also promotes uniform nucleation and planar deposition to inhibit dendrite growth. Furthermore, it can effectively inhibit the dissolution of cathode material in the electrolyte and prevent the infiltration of solvent molecules into the intercalation sites of the cathode material, thereby mitigating their impact on battery capacity and enhancing the stability of cathode circulation. The resulting formation of a stable interface layer can also serve as an efficient protective barrier for preserving the structural integrity and preventing collapse of the cathode material's architecture.

Impressively, at the temperature of −80 °C, asymmetric Zn//Cu cells assembled with ULCE demonstrate stable, long-term cycling for over 5500 cycles at a current density of 1 mA cm^{−2} and over 9000 cycles at a current density of 2 mA cm^{−2} with a high Zn plating/stripping CE. Especially with a high Zn utilization rate of 50% depth of discharge (DoD_{Zn}), the symmetric Zn//Zn cells could maintain stable Zn stripping/plating behaviors for 900 h at −80 °C. When paired with PANI-V₂O₅ cathodes, the full cells exhibit excellent adaptability to wide temperature range from 20 to −80 °C, and wide specific currents from 0.01 to 0.5 A g^{−1} at −80 °C. An impressive ultra-long lifespan of 330 cycles with capacity retention rate of 65% is realized at −80 °C. To further demonstrate its practical application potential, the multi-layered Zn//PANI-V₂O₅ pouch cells with mass loading of 10 mg cm^{−2} are assembled, which exhibit stable and undecayed capacity of 50 mAh g^{−1} for 50 cycles at −80 °C with a specific current of 0.02 A g^{−1}, suggesting its good electrochemical property. In addition, the ULCE strategy can be extended to other kinds of zinc salts. The present study provides an entry point for further investigating and elucidating the colloidal behavior and mechanistic action of CEs in low-concentration salt conditions, thereby expanding the design paradigm of CEs and introducing promising perspectives for safeguarding battery cathode and anode interfaces, which has a reference value for stimulating strategies of colloid utilization.

Results

Concentration-polarization induced phase rigidification

Concentration polarization in batteries arises from the disparity between the local solution concentration near the electrode and the uniform concentration of the bulk solution which is situated at a relatively distant location from the electrode during electrochemical processes. In the liquid colloidal solution, the presence of negatively charged colloidal particles leads to electrostatic repulsion, thereby maintaining a relatively stable colloidal solution system (Supplementary Fig. 1a). Upon interaction with positively charged cations, the charges on the surface of colloidal particles can be easily impaired and neutralized (Supplementary Fig. 1b). Consequently, electrostatic repulsion among the colloidal particles in the colloid solution diminishes, initiating destabilization and particle aggregation (Supplementary Fig. 1c). When the concentration polarization-induced salt concentration at the interface (C_e) surpasses the critical concentration (C_c) of colloidal particles coagulation, it leads to enhanced coalescence between colloidal particles and polymerization of these particles at the electrode interface, resulting in a phase interface formation on the electrode surface (Supplementary Fig. 1d)³⁴. As shown in Fig. 1a, the concentration of Zn²⁺ on the Zn stripping side progressively increases until it surpasses the critical concentration for colloidal particle coagulation in the electrolyte, leading to the formation of condensed colloidal particles on the electrode surface and thereby establishing a compact solidified layer interface layer (Supplementary Fig. 2).

Therefore, the variation in Zn²⁺ concentration at the interface constitutes the fundamental factor underlying the formation of the

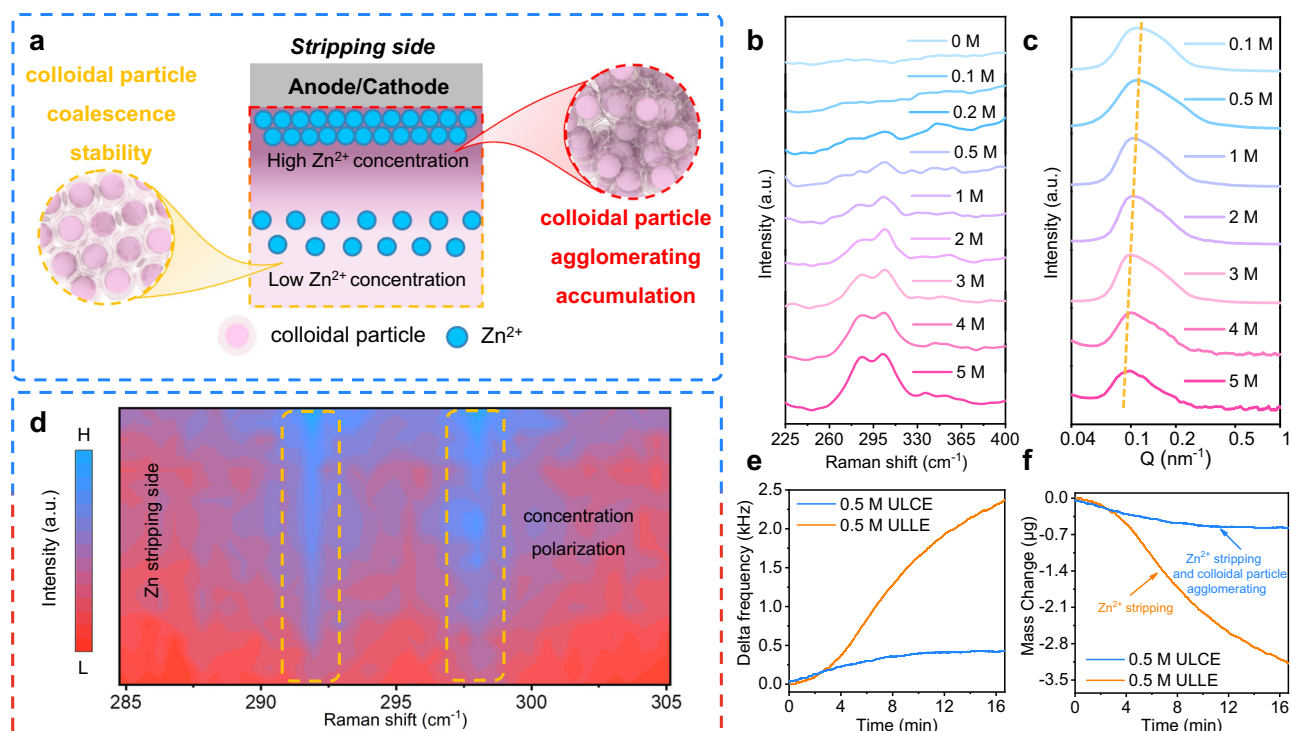


Fig. 1 | Mechanisms underlying the formation of phase interface layers through concentration polarization. **a** Schematic representation of the concentration polarization-induced phase interface layer formation. **b** The Raman and **c** SAXS peaks representing Zn^{2+} solvation configurations and aggregation degree of

colloidal particles at different salt concentrations. **d** In-situ Raman spectra at the electrode/electrolyte interface during Zn depletion. **e** Frequency change and **f** corresponding mass change in EQCM of CP test.

interfacial layer. Primarily, comprehending alterations in solvation structure within electrolytes induced by fluctuations in Zn^{2+} concentration is imperative. Raman spectroscopy was employed to investigate the concentration changes and solvation configurations of Zn^{2+} within various C_{ZnCl_2} electrolytes^{4,35,36}. As depicted in Fig. 1b, in the spectral range of 225–450 cm^{-1} , the 0 M solution shows no discernible peaks around this range. Upon the addition of ZnCl_2 , a distinct peak emerged and exhibited an increasing trend with rising C_{ZnCl_2} , indicating the formation of solvated Zn^{2+} species^{4,37–39}. Notably, the intensities of the peaks increase and the shapes of the peaks change as the concentration continues to rise, providing evidence for a changed coordination mode involving Zn ions. To achieve a more precise species' identification, the solvation structure of electrolytes with varying C_{ZnCl_2} was investigated through molecular simulation (Supplementary Fig. 3). When the concentration is below 0.5 M, solely solvation structures $[\text{Zn}(\text{MeOH})_5\text{Cl}]^+$ and $[\text{Zn}(\text{MeOH})_4\text{Cl}_2]^{2+}$ are observed. When the C_{ZnCl_2} reaches 0.5 M, a solvation structure $[\text{Zn}(\text{MeOH})_3\text{Cl}_3]^{3+}$ emerges. Then, with the continuous increase of concentration, the solvation configuration of zinc ion still changes, and the precise percentage of various Zn^{2+} solvation clusters in the different C_{ZnCl_2} solutions are illustrated in Supplementary Fig. 3.

Consequently, it is imperative to conduct an analysis on the agglomeration of colloidal particle under varying salt concentrations. The change in colloidal particle agglomeration induced by the increase of salt concentration within the system was observed through small-angle X-ray scattering (SAXS), which can clearly distinguish ionic clusters or aggregations at nanoscale, providing evidence for the occurrence of colloidal particle agglomeration in the electrolyte (Fig. 1c)^{40–42}. In the SAXS analysis, the position of the main scattering peak indicates the degree of colloid agglomeration. When the salt concentration is less than or equal to 0.5 M, the scattering peak occurs at -0.115 nm^{-1} , and electrolyte remains mobile (Supplementary Fig. 4a). As the salt concentration increases, there is a gradual shift in the

position of the main scattering peak and narrowing of its shape, indicating an enhanced agglomeration degree of colloidal particles due to changes in solvation structure and increased salt concentration, and the electrolyte undergoes solidification (Supplementary Fig. 4b). The outcome of this experiment predicts that concentration polarization would induce a solid phase interface layer formation at the interface within liquid CEs.

The ratio between Zn^{2+} and Cl^- concentrations can be considered to be precisely equal. Consequently, an increase in Zn^{2+} concentration at the interface leads to a corresponding increase in Cl^- concentration, and the solvation structure formed is consistent with the simulation results. According to the results in Fig. 1b, the in-situ Raman tests conducted at the interface aim to provide evidence for the occurrence of concentration polarization. The schematic diagram of the experimental device is illustrated in Supplementary Fig. 5. The zinc sheet was placed into a pre-prepared specialized electrolytic cell, and 0.5 M ULCE was added. A Raman laser was directed towards the stripping side interface to monitor changes in Zn^{2+} concentration based on variations in Raman signal intensity. As depicted in Fig. 1d, during continuous Zn stripping, the Raman signal intensity gradually increases, providing evidence for an increment in Zn^{2+} concentration at the interface and confirming the occurrence of concentration polarization phenomenon, which would lead to successful formation of a phase rigidification interface layer on the surface of the Zn electrode (Supplementary Fig. 5).

This conclusion is further supported by the electrochemical quartz crystal microbalance (EQCM) tests (Fig. 1e, f, Supplementary Fig. 6). The EQCM test was used to detect mass changes at the nanogram level. The variation of the mass deposited on the quartz crystal exhibits a straightforward linear relationship with the corresponding movement in vibration frequency. Therefore, it can be utilized to further simulate the minute mass variation resulting from the formation and adsorption of interfacial phase rigidification layer on the electrode surface located within the Zn stripping side^{43–45}. It can be

seen that, the frequency in the 0.5 M ULCE system (ultralow-salt-concentration liquid electrolyte without colloidal particles) exhibits significant changes, approaching 2.5 kHz, and the corresponding mass change is also obvious, indicating continuous removal of Zn^{2+} from Zn quartz crystal resonator. Conversely, the frequency change in the 0.5 M ULCE system is minimal. This slight change in mass is suggesting that the removal of Zn^{2+} is accompanied by the formation and adsorption of a solidified layer due to concentration polarization.

The thermal stability of the solidified colloid phase is studied by using differential scanning calorimeter (DSC). There is no obvious change during the temperature range of -80 to 100 °C (super-wide battery application temperature range), confirming the thermal stability of solidified phase composed of colloidal particles SiO_2 (Supplementary Fig. 7). Furthermore, in-situ temperature-change XRD characterization (Supplementary Fig. 8) was used to capture its transformation during the temperature-rising period (from -30 to 100 °C). Specifically, the solidified colloid phase exhibits a constant broad diffraction peak related to amorphous colloidal particles SiO_2 , which reveals that the interface layer could remain stable during temperature-change.

Physicochemical and electrochemical adaptation verification of ULCE toward ultralow temperature

The freezing point (T_f) is a fundamental property of electrolytes used in cold regions. In the case of commonly used solvents like water and many organic solvents, which are molecular crystals, T_f is determined by the strength of self-association interactions governed by secondary bonds such as intermolecular forces and hydrogen bonding. Due to the strong hydrogen bonding networks, water exhibits an unusually higher T_f than other hydrides of group VIA-elements. However, methanol (MeOH), the simplest alcohol with a similar structure to water, displays a significantly lower T_f (-97.5 °C). On one hand, the lack of molecular symmetry in MeOH leads to looser molecular stacking in solid MeOH crystals, resulting in decreased lattice energy compared to ice. On the other hand, steric hindrance caused by the methyl group impedes the formation of hydrogen bonds between -OH groups. Consequently, this is reflected in the remarkably low T_f observed for MeOH. The colloidal solution with colloidal particles dispersed in MeOH exhibits distinct colloidal characteristics. Moreover, it demonstrates excellent temperature adaptability. Consequently, even in low-temperature environments, its intrinsic properties remain unaltered. The investigation of ultra-low temperature “beyond aqueous” CE is thus imperative.

The molecular structure of electrolytes was confirmed using Fourier transform infrared (FTIR) spectroscopy, which enabled the observation of characteristic stretching vibrations associated with different component units (Fig. 2a). The FTIR spectra reveal a significant blue shift in the O-H stretching vibrations, ranging from 3000 to 3500 cm^{-1} , which can be attributed to alterations in hydrogen-bonding environments resulting from the introduction of colloidal particles rich in silicon hydroxyls. By comparing the infrared spectral peak of the MeOH with that of the solution subsequent to sequential addition of colloidal particles and ZnCl_2 , it is worth noting in Supplementary Fig. 9 that the $\nu(\text{C-O})$ stretching located at 1039.7 cm^{-1} in MeOH shifts to 1022.4 cm^{-1} with the addition of colloidal particles and the $\nu(\text{Si-O})$ stretching located at 1117.6 cm^{-1} shifts to 1084.1 cm^{-1} with the addition of ZnCl_2 , thereby confirming the modified Zn^{2+} coordination. These observations indicate that the colloidal particles in the ULCE exhibit remarkable adaptability in coordinating Zn^{2+} , thereby facilitating efficient coordination adjustments²¹.

Not only that, the solvent of the electrolyte, MeOH, has been successfully endowed with the characteristics of exceptional resistance to ultra-low temperatures. As depicted in Fig. 2b, the solidification of 0.5 M ULAE (ultralow-salt-concentration aqueous electrolyte) at -20 °C indicates the loss of fluidity, whereas both 0.5 M ULLE and

0.5 M ULCE retain their flowability even at -80 °C. This observation further substantiates the potential operability of assembled batteries under ultra-low temperature conditions. To demonstrate the cryogenic durability of ULCE, we investigated the solid-liquid transitions of different electrolytes using DSC, which provides specific insights into the thermodynamic changes accompanying temperature variations. Fig. 2c illustrates the heat changes observed in various electrolytes as they were subjected to a temperature increase from -80 to 40 °C. It is found that two electrolytes show various solid-liquid transitions. The 0.5 M ULAE exhibits a pronounced endothermic peak near 0 °C, indicative of its solid-to-liquid phase transition. In contrast, the curve for 0.5 M ULCE remains consistently smooth throughout the entire process, devoid of any discernible state transitions or salt precipitation and dissolution events. These observations underscore the exceptional low-temperature resistance and stability exhibited by this electrolyte.

Apart from preventing electrolyte freezing, the electrochemical performance of the ULCE is also crucial for efficient operation of ZMBs, particularly in terms of its high ionic conductivity and excellent compatibility with zinc anodes. The ionic conductivities of the 0.5 M ULAE and 0.5 M ULCE were evaluated within a temperature range spanning from -80 to 20 °C (Fig. 2d, Supplementary Figs. 10 and 11). Due to the hindered ionic conduction of the fully frozen electrolyte at low temperatures, 0.5 M ULAE exhibits the fast decay of ionic conductivities which is 0.037 mS cm^{-1} at -40 °C. As a comparison, the 0.5 M ULCE shows relatively high ionic conductivity which is 2.42 mS cm^{-1} at -40 °C, and the value remains constant at 0.63 mS cm^{-1} even subjected to extreme temperatures as low as -80 °C. The test results effectively demonstrate the exceptional low temperature tolerance of ULCE.

As previously discussed, the adjustment of Zn^{2+} coordination by colloidal particles weakens the electrostatic interaction between Zn^{2+} and Cl^- or MeOH solvent molecules, thereby facilitating the desolvation process of Zn^{2+} near the electrode/electrolyte interface. The lower activation energy indicates higher temperature independence of the electrolyte, thereby proving its performance at low temperatures. At the stage of subzero temperature, 0.5 M ULCE shows lower activation energy of 20.62 kJ mol^{-1} caused by its unfrozen property and remained robust liquidity down to -80 °C, thus the exceptional thermodynamic performance of ULCE is further demonstrated at ultra-low temperatures (Fig. 2e and Supplementary Fig. 12).

In addition, the suspended colloidal nanoparticles can weak Zn^{2+} -MeOH coordination due to the strong electron affinity between Zn^{2+} and colloidal particle, facilitating fast Zn^{2+} diffusion and desolvation. The unique chemical coordination facilitates the directed migration of Zn^{2+} , thereby leading to a higher Zn^{2+} transference number in the 0.5 M ULCE (0.74) compared to that in the ULLE (0.41, Fig. 2f, Supplementary Fig. 13)⁴⁶. This elevated Zn^{2+} transference number plays a pivotal role in augmenting the electrochemical performance of the Zn anode through three key mechanisms: (1) The Zn^{2+} near the surface of colloidal particle is weakly bounded with solvent molecules, facilitating fast ion diffusion near the solid/liquid interfaces. (2) The solidified layer forms rapid transmission channel for Zn^{2+} , thereby facilitating uniform and efficient Zn^{2+} transmission, and mitigating the concentration gradient at the interface. (3) The solidified layer effectively acts as a barrier, reducing anion concentration in the vicinity of the Zn anode and mitigating corrosion reactions induced by Cl^- ions⁴⁷.

Further use of in-situ cooling Raman spectroscopy was used to differentiate the structure of ULAE and ULCE from room temperature (20 °C) to ultralow temperature (-80 °C) through the utilization of a custom-designed system (Supplementary Fig. 14). The device is designed to be programmable, enabling precise temperature adjustments through the utilization of liquid nitrogen (as low as -100 °C). During the cooling process of ULCE, the peak positions remain unchanged until reaching -80 °C, mirroring the spectrum observed at room temperature. This observation signifies that the electrolyte

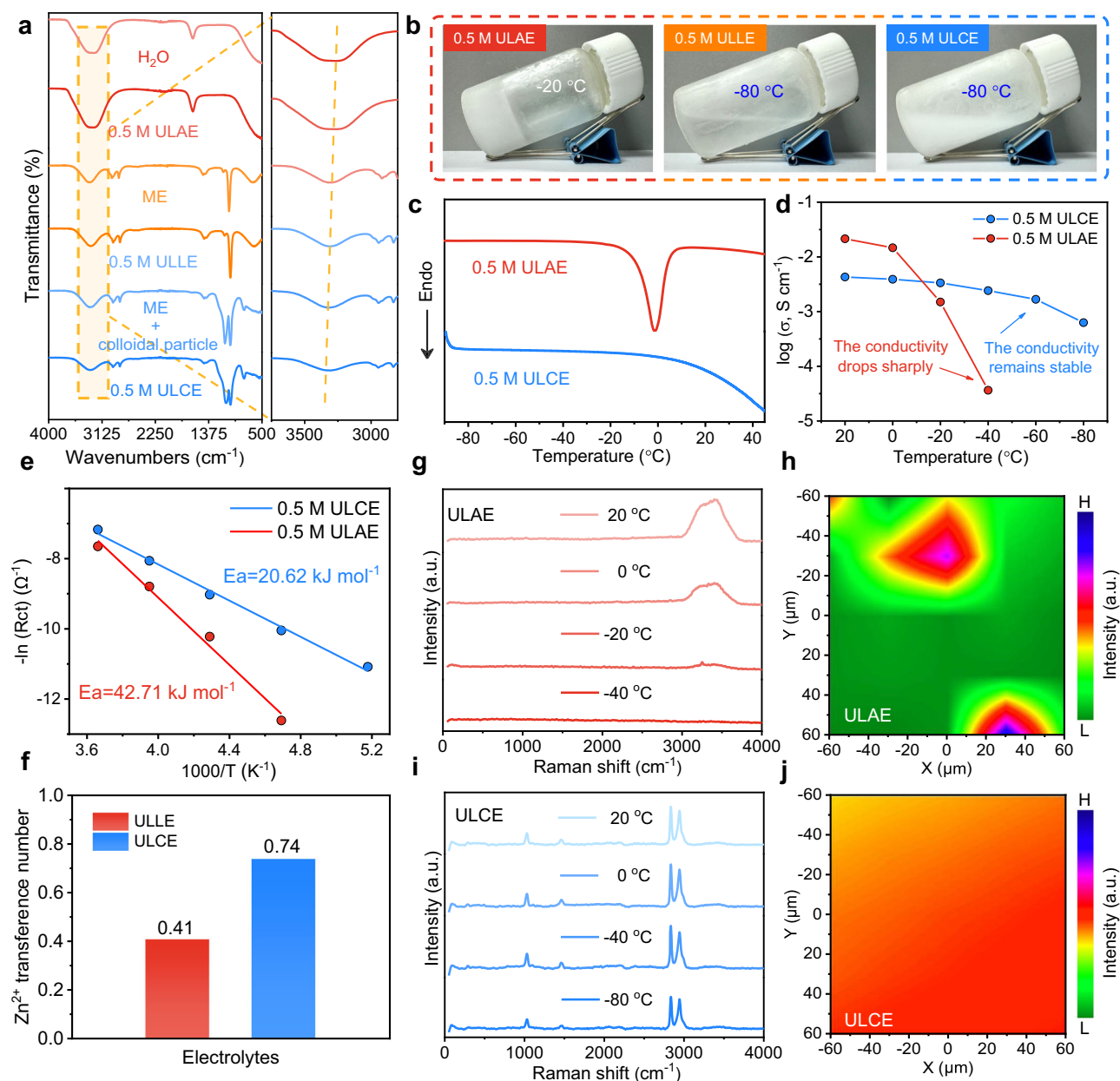


Fig. 2 | The physicochemical and electrochemical adaptation verification of ULCE toward low temperature. **a** FTIR spectra of various solutions and electrolytes. **b** Optical photos of three electrolytes in ultra-low temperature environment. **c** DSC test of ULAE and ULCE from -90 to 45 °C. **d** The ionic conductivities of ULAE and ULCE in the temperature range of -80 to 20 °C. **e** Arrhenius curves and a

comparison of activation energies (E_a) for the de-solvation process of Zn^{2+} in ULAE and ULCE. **f** Transference number of Zn^{2+} in ULLE and ULCE. The in-situ cooling-Raman spectra of **g** ULAE from 20 °C to -40 °C and **i** ULCE from 20 °C to -80 °C. Raman mapping of **h** ULAE and **j** ULCE during the cooling process from 20 °C to -80 °C.

maintains its structural stability even at ultra-low temperatures. The viability of normal operation in a low-temperature environment is further substantiated. Nevertheless, the spectrum of ULAE exhibits a sharp change with the temperature decreases due to freezing, indicating a significant structural transformation (Fig. 2g, i). The peaks in the ULAE spectrum exhibit a significant decrease at -20 °C and completely vanish at -40 °C, indicating that the progressive freezing of ULAE with decreasing temperature results in electrolyte denaturation. This is primarily attributed to the susceptibility of ULAE to freezing at low temperatures, leading to electrolyte denaturation and resulting in non-uniform liquid-solid phase formation.

To visualize the distribution of ULAE and ULCE solution more intuitively, low-temperature Raman mapping was carried out. The color change serves as an indicator of the extent of structural alteration in the electrolytes. Fig. 2h illustrates a pronounced intensity

variation observed in ULAE during the freezing process. As the majority of the electrolyte solidifies, there is a significant discrepancy in strength between the frozen and unfrozen regions. The observed phenomenon can be attributed to the heterogeneous nature of the ULAE. In contrast, it is evident that the ULCE maintains a relatively stable state (Fig. 2j). This phenomenon suggests that the ULCE exhibits exceptional resistance to freezing and demonstrates remarkable stability in its electrolyte structure even under ultra-low temperature conditions.

The self-adaptation verification of ULCE toward Zn anode

Meanwhile, ensuring effective protection at the electrode/electrolyte interface remains a crucial factor for long-term battery operation. The solidified layer induced by concentration polarization can effectively protect the electrode/electrolyte interface. The proposed mechanism

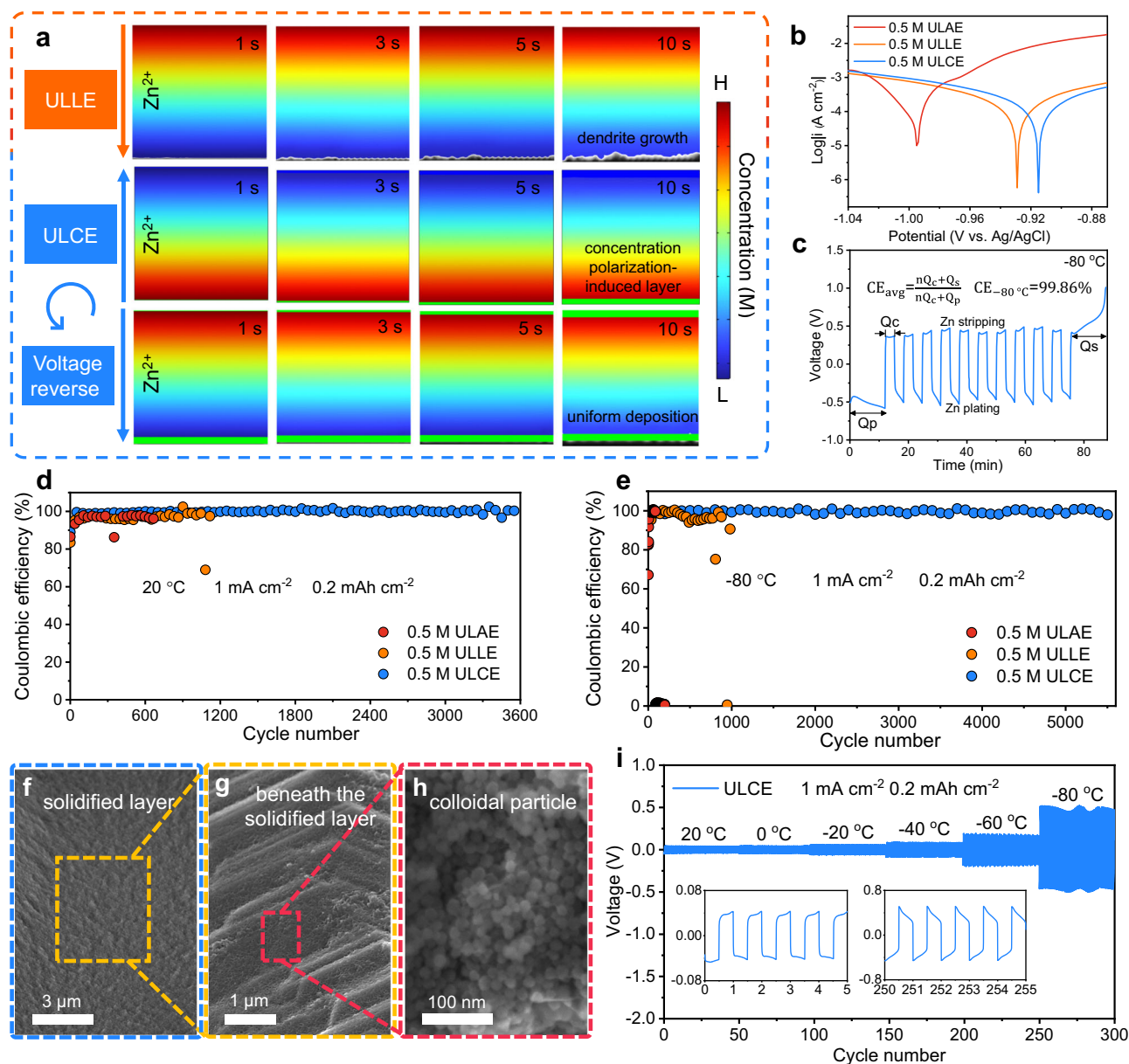


Fig. 3 | The self-adaptation verification of ULCE toward Zn anode. a Phase-field simulations of concentration polarization's effect on ULLE and ULCE. **b** Tafel plots of Zn anode in three electrolytes. **c** The voltage profiles of Zn plating/stripping in asymmetric Zn/Cu cell with ULCE at -80 °C. Long-term cycle performance of Zn//Cu asymmetric cells in both three electrolytes at a current density of 1 mA cm⁻² with

a capacity of 0.2 mAh cm⁻² **d** at 20 °C and an upper cut-off voltage of 0.5 V and **e** at -80 °C and an upper cut-off voltage of 1 V. **f-h** SEM images of solidified layer and Zn deposition morphology after 100 cycles in the ULCE. **i** The voltage profiles of the symmetric Zn//Zn cell testing with ULCE at various temperature at a current density of 1 mA cm⁻² with a capacity of 0.2 mAh cm⁻².

is further substantiated by the phase-field simulation, which incorporates the consideration of mechano-chemical coupling. As depicted in Fig. 3a, the utilization of ULAE and ULLE without colloidal particles leads to dendrite formation due to the inherent non-uniform deposition characteristics of Zn²⁺. In the ULCE electrolyte system, a solidified layer can be formed on the anode surface through concentration polarization during cycling. Firstly, the solidified layer can serve as a solvent barrier, effectively impeding the penetration of solvent molecules to the anode, thereby addressing the issue of hydrogen evolution resulting from direct contact between solvent molecules and anode at the interface. Secondly, the solidified layer generates Zn²⁺ transmission channels that facilitate controlled flow and promote rapid and uniform Zn²⁺ deposition, thereby mitigating uneven deposition issues arising from disorganized deposition caused by excessive Zn²⁺ concentration at the interface. Finally, the high mechanical strength of the interfacial

solidified layer effectively suppresses dendrite formation and mitigates a range of side reactions induced by dendritic growth.

The superior interfacial protection was further assessed through a series of electrochemical tests. The corrosion behavior was investigated using the Tafel test (Fig. 3b). Compared to the use of water as a solvent in ULAE, both ULLE and ULCE exhibit a reduction in corrosion current by approximately one order of magnitude, indicating that MeOH solvent has lower corrosive effects on the Zn anode interface. The corrosion potential of ULCE is slightly higher than that of ULLE, accompanied by a relatively smaller corrosion current, which further confirms that the incorporation of colloidal particles enhances the anti-corrosion capability of the Zn anode.

Additionally, the nucleation behavior of the Zn electrode was investigated by using chronoamperometry (CA). Supplementary Fig. 15 shows the CA plots of the Zn anodes tested in different

electrolytes with a constant overpotential of -150 mV. For the Zn anode in ULCE, the current density quickly reaches equilibrium, indicating a short 2D diffusion process because Zn^{2+} is locally reduced to Zn and the transverse diffusion of Zn^{2+} at the electrode/electrolyte interface has been restricted due to the formation of solidified layer. However, the current density of the Zn anode in ULAE and ULLE exhibits the current rapid growth and fluctuations across the entire range of the curve. The long 2D diffusion process implies the accumulation of Zn^{2+} near the nucleation sites on the Zn anode cycled in ULAE and ULLE, leading to uneven Zn deposition and dendrite growth⁴⁸.

The ULCE employed in this study is expected to exhibit superior electrochemical performance owing to its distinctive properties. Consequently, both asymmetric and symmetric Zn batteries were assembled with the objective of investigating the compatibility of ULCE with Zn. The cyclic voltammetry (CV) curve of asymmetric Zn//Cu batteries at -80 °C exhibits the reversible redox reaction of Zn plating/stripping in ULCE, achieving the highest current density of 0.8 mA cm^{-2} (Supplementary Fig. 16). To accurately quantify the reversibility of Zn plating/stripping in ULCE, we evaluated the Coulombic efficiency of asymmetric Zn//Cu batteries. A conventional practice involves stripping all zinc metal plated onto the current collector in order to determine the Coulombic efficiency for each cycle; however, it should be noted that the Coulombic efficiency of such tests may vary with cycle number. Therefore, we adopted a more refined and innovative approach. In the test, a predetermined quantity of Zn is initially deposited onto the current collector as a “reservoir”, from which a fraction (10–50%) is repetitively stripped and plated for 10 cycles. Subsequently, the remaining Zn capacity is determined by stripping to an elevated upper cut-off potential, such as 1 V. The test results are presented in the Fig. 3c that the high average Coulombic efficiency of 99.86% is achieved -80 °C. The high reversibility can be attributed to that the solidified layer facilitates homogeneous Zn deposition.

Subsequently, a prolonged cycle Coulombic efficiency test was conducted on the Zn//Cu cell to assess the long-term cycling stability of ULCE on the Zn anode. The experiment is initially conducted at a controlled ambient temperature of 20 °C. On account of numerous side reactions such as the formation of dendrites and hydrogen evolution occur in aqueous electrolyte, the Coulombic efficiency of ULAE undergoes a short circuit, resulting in cycle termination at 700 cycles. The stability of the ULLE cycle over an extended period is compromised in the absence of colloidal particles. It causes the Zn//Cu cell using ULLE to suddenly short-circuit when the cycle is about 1200 cycles. The Zn plating/stripping efficiency of the Zn//Cu cell is significantly enhanced in the ULCE, exhibiting an impressive average Coulombic efficiency of 99.73% after 3600 cycles at a current density of 1 mA cm^{-2} , along with a capacity of 0.2 mAh cm^{-2} (Fig. 3d). When the battery's operating temperature plummets to -80 °C under identical current density and capacity conditions, the functionality of the aqueous electrolyte ULAE is compromised by the freezing issue associated with the sharply increased overpotential and battery failure due to the fully frozen electrolyte. The assembled battery is rendered entirely non-functional. Despite the normal functionality of the ULLE assembled cell, achieving a high Coulombic efficiency over long cycles remains challenging. The cell of ULLE undergoes a drastic degradation at the 1000 cycles. On the contrary, the cell of ULCE exhibits high and steady Coulombic efficiency (99.28%) over 5500 cycles (Fig. 3e). This indicates excellent Zn plating/stripping reversibility in the ULCE at different temperatures. When the current density is set at 2 mA cm^{-2} , with a capacity of 0.1 mAh cm^{-2} , the Coulombic efficiency of ULCE is still stable over 9000 cycles (98.85%) at -80 °C (Supplementary Fig. 17). The high Coulombic efficiency and extended cycle life demonstrate the ability of the solidified layer to mitigate undesired side reactions and simultaneously control uniform nucleation and deposition of Zn, thereby enabling a highly reversible anode.

Additionally, post-mortem examinations were conducted to investigate the underlying mechanism responsible for the enhanced stability of the Zn anode in the three electrolytes. Following 100 consecutive plating/stripping cycles, the electrode surface in both ULAE and ULLE exhibits a rough texture characterized by the agglomeration of Zn dendritic, indicating that the uneven deposition of Zn^{2+} leads to an intensified growth of dendrites (Supplementary Figs. 18 and 19). In contrast, the Zn electrode cycled in the ULCE exhibits a distinctively smooth and compact deposition solidified layer, as depicted in Fig. 3f. The cross-section images (Supplementary Fig. 20) demonstrate a microscopically flat layer on the Zn anode with a thickness of $\sim 2 \mu\text{m}$ consisting of agglomerated SiO_2 colloidal particles. Provided that the structural integrity of Zn deposition beneath the interface layer remains intact, the uniform hexagonal basal planes Zn deposition morphology beneath the interface layer can be clearly observed by selectively removing a portion of the solidified layer on the surface (Fig. 3g). When the surface of uniformly deposited Zn is magnified by a factor of 100 K, colloidal particles become distinctly visible (Fig. 3h). In addition, atomic force microscopy (AFM) was used to observe the physical morphologies and Young's modulus. Colloid layers at the electrode interface composed of aggregated colloidal SiO_2 particle (with diameter of 20 nm) demonstrate similarly even surface in the initial cycle and after 100 cycles, and the corresponding Young's modulus values maintain high average values of about 13 GPa, indicating the mechanical hardness and the good physical stability of the solidified colloid layer (Supplementary Fig. 21). The robust and stable physical characteristic can withstand the physical changes, provide the desired mechanical stability during Zn plating/stripping, as well as offer high resistance and enough strength to suppress the Zn dendrite growth^{49,50}. These experimental observations strongly agree with simulation results, supporting the hypothesis that the formation of the solidified layer suppresses whisker growth. This finding further reinforces the pivotal role of ULCE in enhancing Zn electrochemistry.

The cycling stability of Zn anodes is also assessed through prolonged Zn plating/stripping processes in the symmetric battery configuration. As shown in Supplementary Fig. 22, the cells using ULAE fail after only less than 800 cycles, possibly attributed to the occurrence of short circuits induced by dendrites. The ULLE and ULCE cells demonstrate stable cycling performance at ambient temperature. As the temperature plummets to -80 °C, the symmetric cells employing ULLE and ULCE exhibit an increased overpotential due to the diminished ionic conductivity and sluggish Zn plating/stripping kinetics at low temperatures. The ULLE symmetric cells can withstand cycling at -80 °C about 2500 cycles and demonstrates the feasibility of circulating “beyond aqueous” electrolytes at ultralow temperature. Furthermore, the solidified layer formed as a result of concentration polarization phenomenon in ULCE exhibits exceptional structural stability at ultralow temperatures, thereby enabling the symmetrical cell assembly to achieve an impressive doubling of cycle numbers compared to ULLE, with a remarkable endurance of up to 5000 cycles at -80 °C.

The temperature change rate performance of the ULCE electrolyte symmetric cell was further evaluated. As shown in Fig. 3i, the Zn//Zn symmetric cell with the ULCE exhibits stable Zn plating/stripping behaviors across all temperature ranges, indicating that the high ionic conductivity, good Zn compatibility of ULCE, and the formation solidified layer significantly improve the Zn plating/stripping reversibility at different temperatures ranging from 20 to -80 °C. The stability of ULCE at ultra-low temperatures was further assessed through the symmetric battery rate capability test conducted at -80 °C (Supplementary Fig. 23). The current density gradually increases at a rate of 0.5 mA cm^{-2} until it reaches 3 mA cm^{-2} , while the symmetric cell could maintain excellent stability. This further substantiates the practical applicability of ULCE in ultra-low temperature environments and provides additional evidence for the effectiveness and durability of the

ULCE in maintaining a stable electrochemical environment and enhancing the performance of the Zn anode.

The intermittent galvanostatic charge/discharge test enables the occurrence of corrosion reactions at specific intervals of charge and discharge, thereby simulating practical working conditions to accurately reflect actual corrosion behaviors⁴⁸. Under ambient conditions, the symmetric Zn//Zn cells employing the ULLE exhibit recurring performance deficiencies during intermittent charge/discharge testing. After ~430 h of cycling, the overpotential increases to four times that of the initial cycle and continues to rise. This observation suggests that during the intermittent stage, a lack of in-situ generated interface protection layer leads to continuous occurrence of side reactions such as interface corrosion, ultimately resulting in battery failure. In marked contrast, the symmetric Zn//Zn cells employing the ULCE exhibit an exceptionally stable cycle of 2440 h during the intermittent charge/discharge test. Under the protection of the in-situ generated solidified layer, the overpotential remains consistent within a stable range as the number of cycles increases and the prolonged periods of intermittent resting do not yield any additional adverse effects (Supplementary Fig. 24). When the temperature is reduced to -80°C , the symmetric Zn//Zn cells using the ULCE also demonstrate an ultra-stable cycle life, greatly surpassing the mere 400 h achieved by Zn//Zn symmetric cells utilizing the ULLE (Supplementary Fig. 25).

The potential of the ULCE for practical applications at ultralow temperatures was further assessed by conducting additional investigations on the cycle performance of the Zn anode using high DoD_{Zn}. The symmetric battery of ULLE as a reference exhibits a short circuit when subjected to less than 300 h of cycling at a 50% DoD_{Zn}. Remarkably, in the ULCE, the Zn//Zn symmetric cell exhibits a consistently stable cycling performance for over 900 h under 50% DoD_{Zn} (Supplementary Fig. 26). This impressive achievement underscores the promising potential of our ULCE for practical applications.

The self-adaptation verification of ULCE toward PANI-V₂O₅ cathode

The utilization of vanadium oxides as cathodes for rechargeable ZMBs has shown great promise due to the presence of multiple valences of vanadium and a relatively high interplanar spacing⁵¹. Recently, there has been a growing interest in organic materials for low-temperature Zn²⁺ batteries (LTZBs), primarily due to the charge storage predominantly occurring at surface groups and their temperature-independent high capacity. PANI is chosen as the cathode material for constructing LTZBs, relying on the redox mechanism of the benzene/quinone structural transformation and its corresponding ion compensation⁵². Therefore, this work selects PANI-V₂O₅ as cathode material to explore ULCE's application potential in room temperature and ultra-low temperature conditions.

It has been reported that the dissolution of vanadium in electrolytes is a prevalent phenomenon occurring at the interface between the electrolyte and electrode. Consequently, it exhibits significant capacity decay attributed to the dissolution of vanadium during cycling, particularly at low current densities⁵³. Furthermore, the cathode side effects extend well beyond that, exacerbating the situation (Fig. 4a). The divalent nature of Zn²⁺ induces a strong Coulombic interaction with solvent molecules, resulting in the formation of diverse solvation structures. This phenomenon leads to sluggish migration of Zn²⁺ ions and imposes a significant desolvation penalty at the cathode/electrolyte interface due to the pronounced volume effect. During repeated ion intercalation/deintercalation, the lattice spacing undergoes periodic expansion/shrinkage, leading to inevitable volume changes and structural pulverization. The electrostatic interaction between intercalated cations and the host structure poses an insurmountable challenge for achieving reversibility in rocking chair batteries, and the challenge exacerbates in ZMBs due to the high charge density of Zn²⁺. The cathode inevitably undergoes reactions with the electrolyte at the

interface due to its intimate contact. Therefore, the cathode's capacity can be influenced by the incorporation of solvent molecules and other by-products into its structure⁵⁴.

However, the utilization of ULCE electrolytes offers a perfect solution to all aforementioned issues. The concentration polarization-induced solidified layer can be adhered to the cathode surface, facilitating the formation of numerous Zn²⁺ fast transport channels due to colloid agglomeration caused by increased Zn²⁺ concentration. The solidified layer could effectively prevent solvent molecules and byproducts from infiltrating the cathode structure and causing capacity loss externally, while internally inhibiting vanadium dissolution in the electrolyte. Additionally, this phase interface layer safeguards the structural integrity of the positive electrode and prevents its failure resulting from structural collapse. Furthermore, it exhibits an intrinsic electrostatic shielding effect that effectively mitigates Zn²⁺ strong electrostatic impact and successfully addresses side reactions at the cathode interface⁵⁵.

Initially, the vanadium dissolution test was conducted on the PANI-V₂O₅ full cell, which was assembled using three different electrolytes. After 10 cycles process, the cells were disassembled, and the vanadium dissolution in the electrolyte was analyzed, followed by subsequent Inductively Coupled Plasma Atomic Emission Spectrometry (ICP-AES) testing on the aforementioned electrolytes. The results are summarized in Fig. 4b. The concentrations of vanadium in the three electrolytes, ULAE, ULLE, and ULCE after cycling are measured as 6.82 ppm, 9.5 ppm, and 1.2 ppm respectively. It is observed that the solubility of vanadium in MeOH solvent-based ULLE is higher compared to water solvent-based ULAE, indicating a greater likelihood of vanadium dissolution in the MeOH-based electrolyte solution. Furthermore, it is found that the concentration of vanadium in ULCE containing colloidal particles is significantly lower than that in the other two electrolytes, suggesting an effective prevention of vanadium dissolution through the formation of a solidified layer.

To further validate the vanadium dissolution of the three electrolytes, three PANI-V₂O₅ electrode sheets with identical loadings were immersed in the respective electrolytes. Notably, for ULCE, the electrode sheets were subjected to a simple deposition cycle prior to immersion, resulting in the formation of a solidified layer. Supplementary Fig. 27a displays the condition of the three electrolytes after soaking PANI-V₂O₅ cathode for 7 days. The ULAE and ULLE exhibits distinct yellow coloration after 7 days of immersion with the PANI-V₂O₅ electrode, and the situation in ULLE is much worse. On the contrary, the ULCE shows negligible color change throughout the soaking period. The vanadium concentrations results are summarized in Supplementary Fig. 27b. Specifically, the vanadium concentrations in the ULAE, ULLE and ULCE are found to be 36.5 ppm, 47 ppm and 3.5 ppm, respectively. It should be noted that the concentration of dissolved vanadium ions in ULAE and ULLE is similar, but the color of ULAE is lighter, indicating that the dark color in ULLE does not solely come from vanadium ions. FTIR test manifests that the severe color change in ULLE is due to the partial dissolution of organic component PANI in ULLE (Supplementary Fig. 27c)^{56–59}. This result demonstrates that the formation of a solidified layer in ULCE could inhibit both vanadium and PANI leaching, further confirming its important role in maintaining the stability of the cathode materials.

Next, we initially assessed the low-temperature electrochemical stability windows of two types of ultra-low temperature-resistant electrolytes in preparation for subsequent ultra-low temperature cycling of the full cell⁶⁰. We evaluated the electrochemical windows of ULLE and ULCE at -80°C using linear scan voltammetry (LSV) (Supplementary Fig. 28). The ultralow-temperature environment widens the cathodic limits of the electrolyte by inhibiting highly active solvents, resulting in a significant suppression of the oxidation potential with an extensive window of 2.75 V. Concurrently, the ULCE exhibits a slight increase in oxidation potential and a diminished current

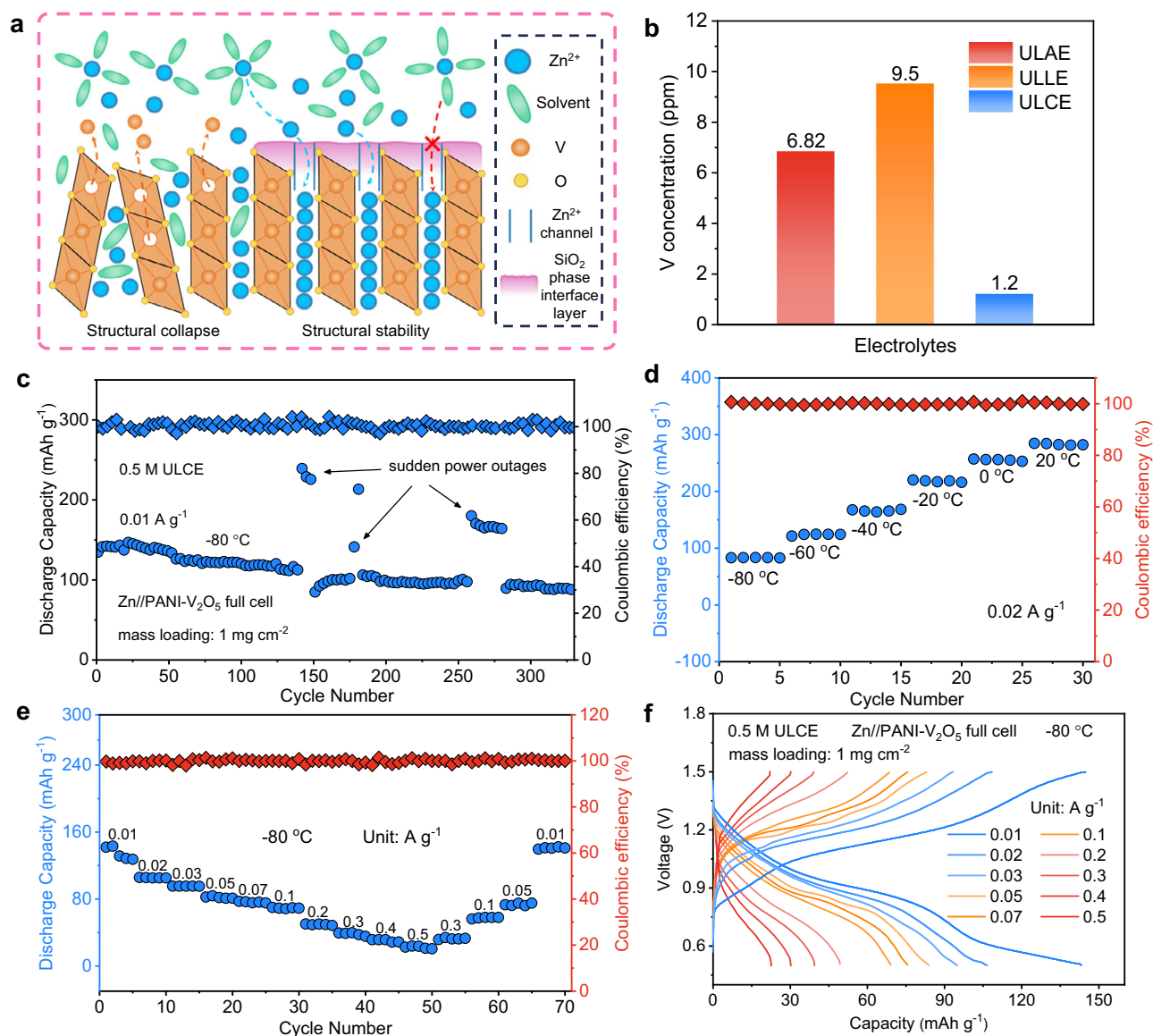


Fig. 4 | The self-adaptation verification of ULCE toward PANI-V₂O₅ cathode. **a** Current challenge arising in V-based cathode and the mechanism of solidified layer to improve the structural stability. **b** The concentration of V ions in the electrolyte after 10 cycles with three different types of electrolyte. **c** The cycling

ability of PANI-V₂O₅ full cell with ULCE at -80 °C. **d** The capacity ability of PANI-V₂O₅ full cell with ULCE at various temperatures. **e** The rate performance of cells with ULCE at -80 °C and **f** corresponding charge and discharge curves.

response compared to ULLE, which can be attributed to the influence exerted by colloidal particles. The suppressed side effect is beneficial for stable cycling under ultra-low temperature conditions.

The efficacy of this strategy was further confirmed in Zn//PANI-V₂O₅ full cells. The PANI-V₂O₅ cathodes, with a mass loading of -1-mg cm⁻² was assembled with ULAE, ULLE and ULCE and Zn metal. The initial discharge capacity of the ULAE full cell at room temperature is 304.7 mAh g⁻¹, however, due to inherent limitations in the electrolyte properties, issues such as dissolution of vanadium and collapse of cathode structure lead to a decay in capacity (Supplementary Fig. 29b). After undergoing 40 cycles, the battery's capacity diminishes to 75.6 mAh g⁻¹, resulting in a mere capacity retention rate of 24.8%. What's worse, the battery will be fails due to electrolyte freezing when the temperature drops to -80 °C. The performance of the ULLE-assembled full cell is also not promising (Supplementary Fig. 29c). At room temperature, the discharge capacity decreased from 280.1 mAh g⁻¹ to 66.3 mAh g⁻¹ (40th cycle), resulting in a capacity retention rate of only 23.7%, which may be attributed to the higher

solubility of vanadium and organic polymer in the cathode material in ULLE batteries. Conversely, stable cycling could be achieved with ULCE. It is noteworthy that the curing layer formed by concentration polarization at the cathode interface not only effectively mitigates the occurrence of cathode side reactions in the battery but also significantly enhances its capacity retention rate. After 40 cycles, the ULCE full cell discharge capacity decreases from 293.8 mAh g⁻¹ to 170.1 mAh g⁻¹, resulting in a capacity retention rate of 57.9%, indicating a significant level of capacity preservation compared to ULAE and ULLE (Supplementary Fig. 29a). When the temperature is lowered to -80 °C, the discharge capacity decreases to 134.8 mAh g⁻¹ at specific current of 0.01 A g⁻¹. After undergoing 330 cycles in the ultra-low temperature environment, the discharge capacity is observed to 87.6 mAh g⁻¹, with a corresponding capacity retention rate of 65.0%, demonstrated high-capacity retention levels (Fig. 4c). The aforementioned result is in accordance with the charge/discharge curves (Supplementary Fig. 30).

The variable temperature rate test of the ULCE full cell was conducted at an ultra-low specific current of 0.02 A g⁻¹. To mitigate abrupt

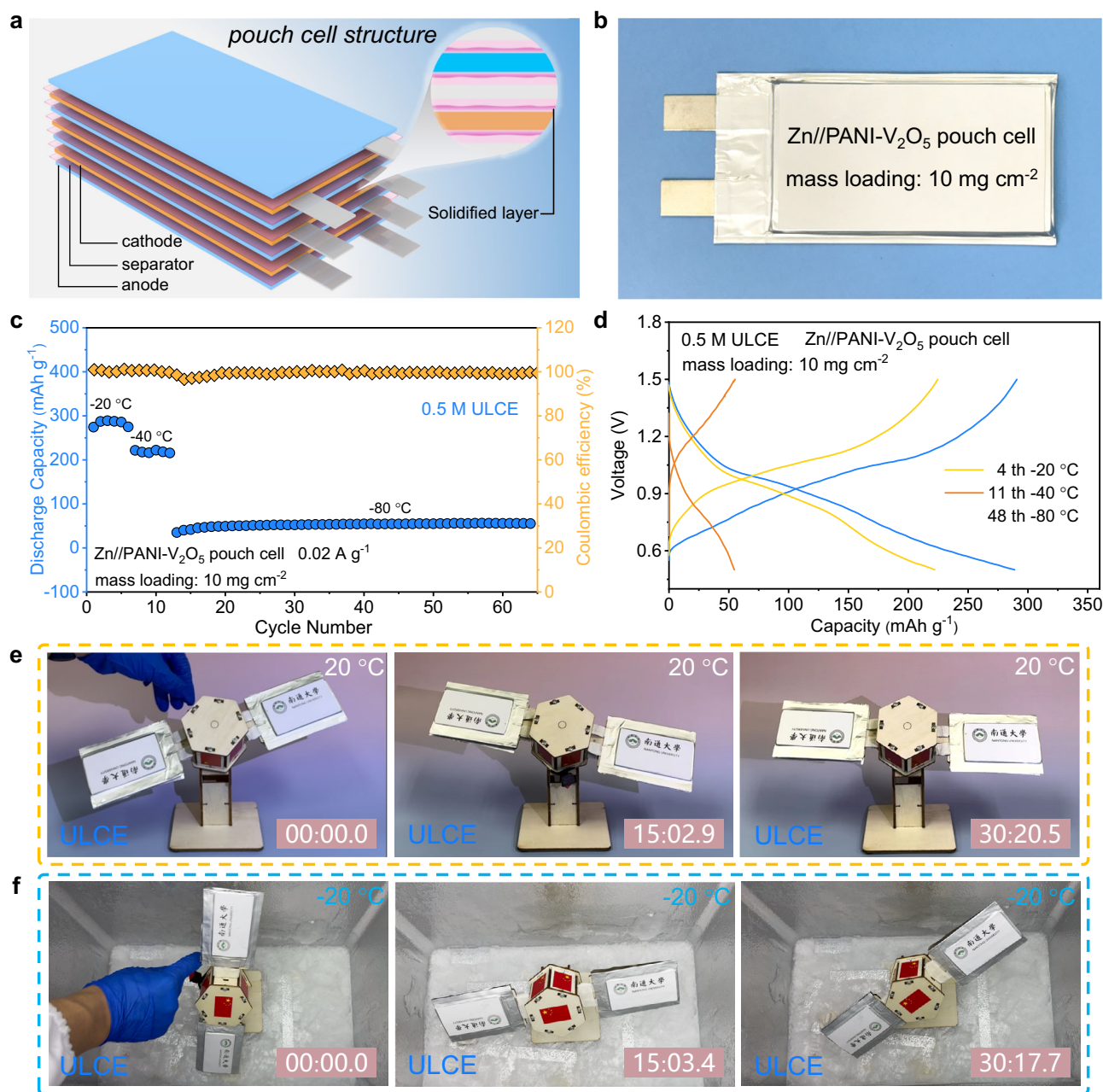


Fig. 5 | The performance and physical demonstration of pouch cells. **a** Structure and interface mechanism of multi-layer pouch cell. **b** Physical diagram of a pouch cell with mass load of 10 mg cm^{-2} . **c** Long-term cycle performance of multi-layer

pouch cell with ULCE at various temperatures and **d** corresponding charge and discharge curves. Schematic illustration of four pouch cells-powered satellite models at **e** 20 and **f** -20°C with ULCE.

temperature fluctuations in the test device, it is recommended to adopt a gradual increase with intervals of 20°C , starting from -80°C and ascending to 20°C (Fig. 4d). The battery's discharge capacity aligns perfectly with expectations across all temperature ranges, exhibiting exceptional performance at both -80°C and 20°C . This further validates the authenticity of the findings across other temperature intervals, demonstrating that the ULCE-assembled battery is highly adaptable to varying temperatures. To investigate the ULCE in practical applications at -80°C of rate performance with different current density, full cells based ULCE were assembled and tested. The rate performance of the cells at various specific currents from 0.01 to 0.5 A g^{-1} is illustrated in Figs. 4e, f, demonstrating the remarkable discharge capacity exhibited by the battery with the ULCE across different current densities. The exceptional rate performance fulfills the practical application discharge requirements in ultralow temperature environments.

To further illustrate the practical application potential of the ULCE, we fabricated and conducted performance testing on pouch cells (mass loading: 10 mg cm^{-2})^{61,62}. The assembly of the pouch cell is illustrated in Fig. 5a, b. By harnessing the concentration polarization effect of ULCE during cycling, the solidified layer can be formed at the electrode interfaces of pouch cell, effectively enhancing its performance. We assembled a multi-layered Zn//PANI- V_2O_5 pouch cell⁶³, which exhibit a specific capacity about 300 mAh g^{-1} at the specific current of 0.02 A g^{-1} and temperature of -20°C . Then, the temperature is reduced to -40°C without altering the current density, resulting in a decrease in the pouch cell capacity to 221.6 mAh g^{-1} and the capacity retention rate remains consistently high. To evaluate the cycling performance under lower temperature conditions, the temperature is further decreased to -80°C . The capacity stabilizes and maintains a consistent level of 50 mAh g^{-1} , and an impressive capacity

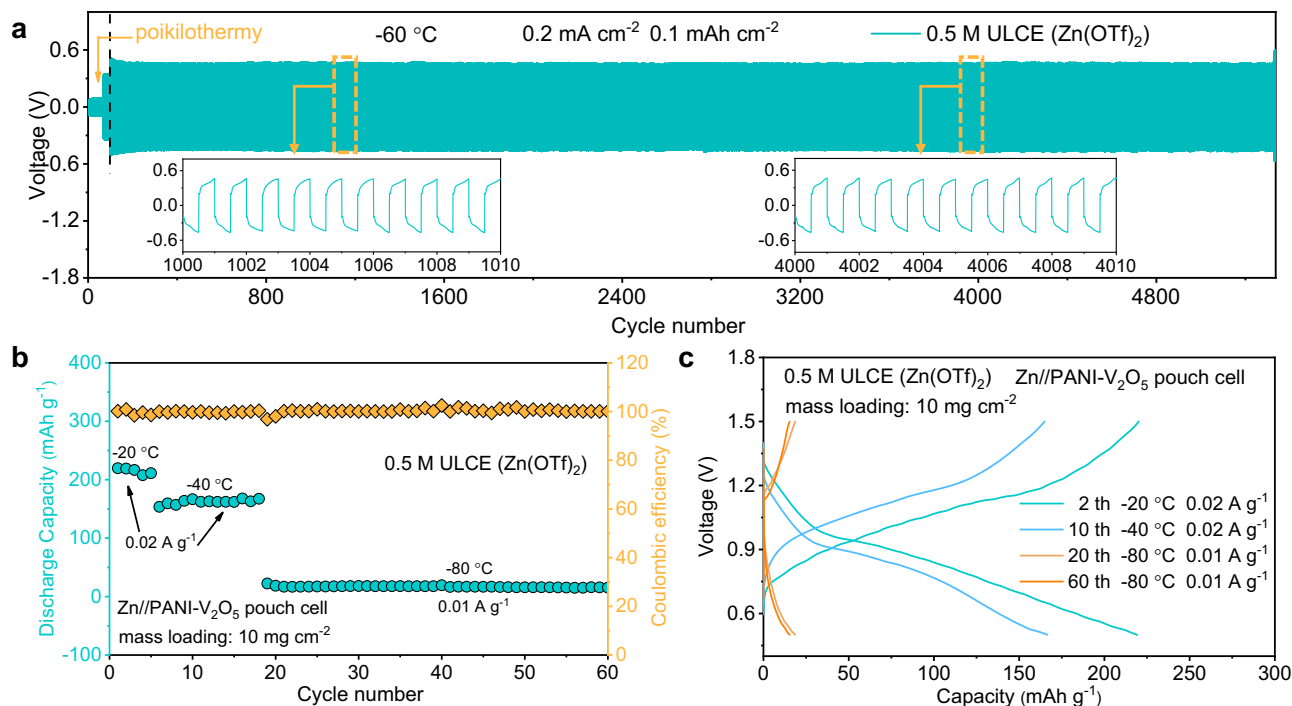


Fig. 6 | Universal effect of different anionic salts. a Long-term cycle performance of Zn/Zn symmetric cells in ULCE (Zn(OTf)₂) at a current density of 0.2 mA cm⁻² with a capacity of 0.1 mAh cm⁻² at -60 °C. **b** Long-term cycle performance of single

piece of pouch cell with ULCE (Zn(OTf)₂) at various temperatures and **c** corresponding charge and discharge curves.

retention rate of 100% could be observed after 50 cycles, demonstrating excellent electrochemical performance (Fig. 5c, d). The results demonstrate its robust cycle performance even under practical high-loading conditions. To assess the practical application capability of ULCE pouch cell⁶⁴, we conducted experiments to evaluate the endurance performance of a satellite model powered by these cells under different temperature conditions. At 20 °C, the low-speed rotating satellite model can be powered by four series of single-layered pouch cell (mass loading: 10 mg cm⁻²) for over 30 min (Fig. 5e, Supplementary Movie 1), which demonstrates the ULCE pouch cell's exceptional practical applicability. Whether the physical rotation of pouch battery would affect the mass transfer of the electrolytes is an interesting question that needs to be considered, which is important for its practical use under dynamic conditions. The operation of the pouch cells with ULCE and ULAE as the wing of satellite model are also conducted (Supplementary Fig. 32, Supplementary Movie 2 and 3), whose operating time are a little shorter than that for ULCE. Furthermore, a homemade device is designed that can test a rocking battery to more intuitively observe the effect of rotation on the battery operation (Supplementary Fig. 33, Supplementary Movie 4). The charge/discharge profiles of static and side-to-side oscillated pouch cells with different electrolytes are listed in Supplementary Fig. 34. It can be seen that the charge/discharge curves of all three batteries are smooth in the static state. However, the charge/discharge curves of oscillating batteries with ULAE and ULCE demonstrate observable voltage oscillation due to the interface disturbance in all-liquid electrolytes. For ULCE, due to the formation of solidified layer at the interface, its effect on mass transfer could be effectively inhibited, contributing to the smooth voltage curves and longer operating time under dynamic condition. The results indicate our electrolyte ULCE for ZMBs is potential not only for stationary large-scale energy storage, but also for dynamic energy storage. Furthermore, when the temperature is decreased to -20 °C, the endurance time of the satellite model exhibits minimal variation compared to that at 20 °C (Fig. 5f, Supplementary Movie 5). The ULCE-based pouch cell exhibits exceptional resistance to

low temperatures, thereby showcasing its immense potential for practical applications in cold environments.

Universal effect of different anionic salts

The success of “beyond aqueous” ULCE in reinforcement of ultra-low temperature cycling performance and enhancement of anodic and cathodic interface stability in ZMBs motivate us to assess its universality for different anionic zinc salts. We thereby synthesized four additional ULCE, with different zinc salts of Zn(OTf)₂, ZnSO₄, Zn(ClO₄)₂, Zn(AC)₂ respectively (Supplementary Fig. 35). In addition to the limited solubility of ZnSO₄ in MeOH, the other three zinc salts exhibit favorable solubility in MeOH. Subsequently, we chose ULCE (Zn(OTf)₂) as the subject of investigation to thoroughly examine its electrochemical performance and validate its applicability. Firstly, we investigate the cyclic performance of Zn//Zn symmetrical cell to assess the protective effect of the phase interface on the anode. Despite the symmetrical cell employing the 0.5 M ULCE (Zn(OTf)₂) exhibits an increased overpotential due to reduced ionic conductivity and sluggish Zn plating/stripping kinetics at low temperatures, it demonstrates stable operation at -60 °C for over 5000 cycles, indicating remarkable temperature stability (Fig. 6a).

The wide electrochemical window (Supplementary Fig. 36) of ULCE (Zn(OTf)₂) at the temperature of 20 °C demonstrates its feasibility in full cells. To further validate its universality, we developed a pouch cell (mass loading: 10 mg cm⁻²) with ULCE (Zn(OTf)₂) for comprehensive testing. The pouch cell exhibits capacity of 219.7 mAh g⁻¹ at -20 °C and the capacity retention rate reached 96.2% after undergoing 5 short cycles. As the temperature decreases to -40 °C, the battery capacity reaches 153 mAh g⁻¹ under constant current conditions, and after -13 cycles, it increases to 167.4 mAh g⁻¹ while maintaining a high percentage of 100% Coulombic efficiency. As the temperature is reduced to -80 °C, accompanied by a decrease in specific current to 0.01 A g⁻¹, the battery capacity decreases to 22.4 mAh g⁻¹. After subjecting the pouch cell about 50 cycles at this ultra-low temperature, an impressive stable operation can be observed, thus proving its

feasibility in ultra-low temperature environment (Fig. 6b, c). The capacity difference of ULCE ($\text{Zn}(\text{OTf})_2$) and ULCE (ZnCl_2) can be attributed to the intrinsic difference in ionic conductance between the two salts. These test results provide strong evidence for the universality of the formation of solidified layer and its protective effect across various anionic zinc salts.

Discussion

In summary, a promising strategy is proposed to design “beyond aqueous” CEs with ultra-low salt concentration for ultra-low temperature ZMBs. Due to the phenomenon of concentration polarization in a low salt concentration environment, the intrinsic cohesion stability of colloidal particles at the electrolyte/electrode interface is disrupted, leading to spontaneous in-situ generation of an interfacial phase rigidification layer on both cathode and anode surfaces. This enables protection for both electrodes: preventing dendrite growth and achieving stable Zn deposition on the anode side, while inhibiting dissolution of cathode material, maintaining its structural stability, and facilitating uniform Zn deposition through nano transfer channels on the cathode side. Moreover, by utilizing MeOH as a “beyond aqueous” solvent, normal circulation can be achieved even under ultra-low temperature conditions down to -80°C . Furthermore, ULCE are prepared using different zinc salts, which demonstrates the universality of concentration-polarization induced phase rigidification in different ultralow-salt-concentration colloid electrolytes.

Most importantly, through the investigation of colloidal particles' unique behavior at ultra-low salt concentrations, we have successfully elucidated the crucial role played by CEs in such conditions. Employing ultra-low salt concentration CEs can serve as a straightforward and universal approach to transform the adverse interfacial concentration polarization during battery cycling into an advantageous driving force for the formation of an interfacial protective layer, thereby achieving comprehensive protection for both cathode and anode. This principle has been applied to the fabrication of quasi-solid electrolytes in our previous work²⁴, in which high concentration salt can disrupt the stability of colloidal particles leading to the formation of solid electrolytes. Furthermore, the phenomenon of concentration polarization is ubiquitous in all kinds of electrolytes and battery systems. Therefore, its possible effects in different battery types and electrolyte types can be thoroughly studied in the future, including but not limited to liquid/solid electrolytes of Zn-based batteries. Finally, we expect that the development of ultra-low salt concentration CEs will facilitate (1) a deeper comprehension of concentration polarization at the electrode/electrolyte interface, (2) a design paradigm of investigating and elucidating the variable and dynamic colloidal behaviors and mechanistic actions of CEs, (3) a widespread and uncomplicated strategy for electrolyte design, and (4) an inspiration for designing other side reactions during battery cycling that can act as favorable driving forces.

Methods

Materials

Zinc chloride (ZnCl_2 , $\geq 96\%$), zinc perchlorate ($\text{Zn}(\text{ClO}_4)_2$, 98%), zinc sulfate (ZnSO_4 , AR), zinc trifluoromethanesulfonate ($\text{Zn}(\text{OTf})_2$, 98%), zinc acetate ($\text{Zn}(\text{AC})_2$, 99%), vanadium pentoxide (V_2O_5 , 99.99%), H_2O_2 , aniline, KOH were produced by Shanghai Aladdin Bio-Chem Technology Co., Ltd. All chemicals were used without further purification. Zn metal foils (200 μm , 10 μm) and Cu foils (10 μm) were supplied by Shanghai Weidi Metal Material Technology Co., Ltd. The stainless-steel mesh (400 mesh) was supplied by Guangdong Canrd New Energy Technology Co., Ltd.

Preparation of different electrolytes

The ULAE was prepared by combining salt and deionized water to achieve a salt concentration of 0.5 M. Similarly, the ULLE was prepared

by mixing salt with MeOH to obtain a salt concentration of 0.5 M. And the ULCE involved adding salt to a pre-obtained colloidal silica solution in order to attain a salt concentration of 0.5 M. The preparation method for various salts remains consistent. If not specified, the colloid content in the CE is 10 wt%.

Synthesis of PANI- V_2O_5

Typically, 0.72 g of V_2O_5 powder was dissolved in a mixture solution containing 60 mL of DI water, 10 mL of H_2O_2 (30 wt.%) to obtain a homogeneous clear orange solution. Then the mixture was sealed into a 100 mL Teflon-lined stainless-steel autoclave and heated at 190°C for 10 h to produce the hydrated V_2O_5 hydrogel. Then, the prepared hydrated V_2O_5 hydrogel was transferred into a beaker with aniline monomers (720 μL , slowly dripped) by vigorously stirring at room temperature. During the process, dark blue precipitate can be produced. The precipitates were isolated and washed by filtration with DI water and ethyl alcohol for several times, followed by getting freeze-dried under -40°C for 24 h to obtain the final product³¹.

Preparation of the PANI- V_2O_5 cathode electrode

To prepare the PANI- V_2O_5 cathode electrode, PANI- V_2O_5 active material, super P and polyvinylidene difluoride were blended in a mass ratio of 7:2:1 and mixed with NMP solvent. The obtained electrode slurry was coated on stainless-steel mesh collectors and then dried at 70°C overnight to remove residue solvent. The cathode of the pouch cell is coated with slurry on a stainless-steel collector, which is securely held in place by a custom bracket (Supplementary Fig. 31). The areal mass loadings of coin cell and pouch cell were controlled at about 1 and 10 mg cm^{-2} , respectively.

Activation energy calculation

The activation energy (E_a) for interfacial charge transfer tested with Zn//Zn symmetrical batteries follows the Arrhenius equation as follows equation (Eq. (2)):

$$\frac{1}{R_{ct}} = A \exp\left(\frac{-E_a}{RT}\right) \quad (2)$$

where A is the frequency factor, R is the gas constant, and T is the absolute temperature. The R_{ct} values at each temperature were estimated from the corresponding equivalent circuit fit.

Steady-state cation transference number calculation

To accurately calculate the steady-state cation transference number (t_{ss}^+), each sample cell should be subjected to a conditioning treatment, which consists of five charge and discharge cycles at a low current density of 0.06 mA cm^{-2} in order to help stabilize the electrodes' interfacial layer. After the preconditioning, constant polarization potential (ΔV) is applied until the steady-state current (i_{ss}) is reached. Bulk and interfacial resistances are measured by performing AC impedance spectroscopy before the polarization and during the steady-state. The calculating equation is listed as below (Eq. (3))^{65–70}:

$$t_{ss}^+ = \frac{i_{ss}(\Delta V - R_o i_{ohm})}{i_{ohm}(\Delta V - R_{ss} i_{ss})} \quad (3)$$

in which R_o is the initial interfacial resistance, R_{ss} is the interfacial resistance when i_{ss} is reached. i_{ohm} is defined as an initial current calculated by Ohm's law, given by the following equation (Eq. (4)):

$$i_{ohm} = \frac{\Delta V}{R_T} \quad (4)$$

where ΔV is the applied polarization potential and R_T is the total initial cell resistance.

Materials characterizations

The chemical structures of samples were examined by FTIR spectrometer (ThermoFisher, Nicolet IS10). All the morphologies' observation was conducted by Scanning Electron microscopy (SEM, ZEISS Gemini SEM 300). SAXS using Cu-K α radiation was employed to test the electrolytes. The Raman spectra were collected on Laser Confocal Raman Micro spectroscopy (Horiba Jobin Yvon, France). For the in-situ Raman test, the Raman beam is focused on the neighborhood of Zn prolapsed side, and the initial measured results are from the bulk electrolyte. With the beginning of the cycle, concentration polarization leads to an increase in zinc ion concentration at the Zn²⁺ outflow interface, consequently inducing changes in the solvation structure of the electrolyte. Therefore, the in-situ Raman signals' changes refers to ion's concentration changes in the neighborhood of electrode/electrolyte interface during the Zn stripping, which could reliably imply the ion distribution changes. For Raman mapping, ULAE is cooled from 20 to -40 °C and ULCE is cooled from 20 to -80 °C to observe whether phase transition process would take place in the two electrolytes during the cooling process. DSC was carried out in DISCOVERY DSC250 with a cooling rate of 10 K min⁻¹, constant temperature for 2 mins and a heating rate of 5 K min⁻¹. In-situ temperature-change X-ray diffraction (XRD) characterization was conducted on diffractometer (Bruker, D8 Advance). AFM was used to observe the physical morphologies and Young's modulus (Bruker, Dimension Icon). The element concentrations in the electrolytes were determined by ICP-AES (Agilent 5800).

Electrochemical characterizations

Zn foils with a thickness of 200 μm were used in cells if not mentioned, while the cells under 50% DoD_{Zn} was conducted by using Zn foil with a thickness of ca. 10 μm . The total capacity of the used Zn foil (C_{zn}) is calculated based on the mass of the Zn foil (m_{zn}) according to the following equation (Eq. (5)):

$$C_{zn} = m_{zn} \times 820 \text{ mAh g}^{-1} \quad (5)$$

Before use, the Zn foil was polished by softback sanding sponges and then wiped with ethanol. The used separator was glass fiber separator (Whatman, GF-A, 260 μm). The electrochemical tests were carried out in coin-type cell (CR2032) and pouch cell. During cell assembly, the Zn//Cu coin cells were assembled using Cu foil ($\Phi 12\text{mm}$) as cathode and zinc foil ($\Phi 12\text{mm}$) as anode. The Zn//Zn coin cells were assembled using zinc foil ($\Phi 12\text{mm}$) as cathode and anode. For coin full cells, zinc foil ($\Phi 12\text{mm}$) was used as the anode, and the stainless-steel mesh with PANI-V₂O₅ load is cut into a small round ($\Phi 12\text{mm}$) as the cathode. The diameter of separators used in coin cells is 16 mm. For pouch cells, zinc foil and the stainless-steel mesh with PANI-V₂O₅ load were cropped to a rectangle of 4.1 \times 7.6 cm as the anode and cathode, and both tabs were made of Ni. The separator was cropped to a rectangle of 4.5 \times 8 cm. The electrolyte dosage of coin cells was 100 μL . In the pouch cell, the electrolyte dosage of each cathode plate was 1 mL. During the assembly of the multi-layered pouch cell, four anode plates and three cathode plates were stacked together, as shown in Fig. 5a. All batteries were tested using the Neware battery test platform (CT-4008Q-5V100mA). The voltage range for ULCE (ZnCl₂) full batteries was 0.5–1.2 V at room temperature and 0.5–1.5 V at subzero temperatures, while for ULCE (Zn(OTf)₂) full batteries, the voltage range was consistent at 0.5–1.5 V across all temperatures. The specific capacity of full batteries was calculated based on the mass of PANI-V₂O₅. The electrochemical tests were carried out in a climatic chamber to realize specific environmental temperatures (a range of 20 to -80 °C).

The Tafel plots were recorded by electrochemical station within a voltage range of -1.04 V ~ -0.87 V in a three-electrode system (Ag/AgCl as reference electrode, Pt as counter electrode, Zn as working electrode) at room temperature. CA measurements are conducted in Zn//

Zn symmetric cells with a bias voltage of -150 mV over 250 s at room temperature. The CV curve of asymmetric Zn//Cu batteries were tested within a voltage range of 1 to -0.6 V at a scan rate of 0.1 mV s⁻¹ at -80 °C. The electrochemical windows of electrolyte ULCE (ZnCl₂) and ULLE (ZnCl₂) were tested by linear sweep voltammetry (LSV) measurements within a voltage range of 0–3 V at a scan rate of 1 mV s⁻¹ in a Zn//Ti coin cell at -80 °C. The electrochemical windows of electrolyte ULCE (Zn(OTf)₂) was tested within a voltage range of 0–2 V at a scan rate of 1 mV s⁻¹ in a three-electrode system (Ag/AgCl as reference electrode, two Pt as working and counter electrode respectively) at room temperature. The ionic conductivities of the electrolytes were calculated according to electrochemical impedance spectroscopy (EIS). The Zn²⁺ conductivities were calculated according to the following equation (Eq. (6)):

$$\sigma = \frac{d}{RS} \quad (6)$$

where d is the thickness of electrolyte between blocking electrodes, R is the bulk resistance, and S is the contact area. These measurements were tested on electrochemical workstation (CHI 660E, Chenghua Shanghai, China).

EQCM measurements

EQCM measurements were carried out on CHI400C. An AT-cut Pt-coated quartz crystal with the resonance frequency of 5 MHz was coated with Zn and used as the working electrode. Zn foil was used as a counter and the reference electrode. The EQCM result was performed at room temperature in galvanostatic mode with low current of 1 mA. The Δm_{ss} of working electrode was calculated from the change in resonance frequency using the equation (Eq. (7)):

$$\Delta f = \frac{-2f_o^2 \Delta m}{[A \cdot \text{sqrt}(\mu\rho)]} \quad (7)$$

where f_o is the basic resonant frequency of the crystal (7.995 MHz), A is the area of the Zn plated on the crystal (0.196 cm²), ρ is the density of the crystal (2.684 g cm⁻³), and μ is the crystal shear coefficient (2.947×10^{11} g cm⁻¹ s⁻²). According to the calculation based on the aforementioned data, there is a correspondence between a change in frequency per Hz and a mass change of 1.34 ng.

Computational studies

MD simulations are performed with Gromacs 2019.6⁷¹. For analysis of solvation structure with different salt concentrations, the simulation system with 0.1 M ZnCl₂ is composed of 8 Zn²⁺, 16 Cl⁻, 1875 MeOH; the simulation system with 0.2 M ZnCl₂ is composed of 16 Zn²⁺, 32 Cl⁻, 1875 MeOH; the simulation system with 0.5 M ZnCl₂ is composed of 39 Zn²⁺, 78 Cl⁻, 1875 MeOH; the simulation system with 1 M ZnCl₂ is composed of 78 Zn²⁺, 156 Cl⁻, 1875 MeOH; the simulation system with 2 M ZnCl₂ is composed of 156 Zn²⁺, 312 Cl⁻, 1875 MeOH; the simulation system with 5 M ZnCl₂ is composed of 390 Zn²⁺, 780 Cl⁻, 1875 MeOH. The above species are uniformly mixed by PACKMOL⁷². Cl⁻, MeOH are modeled by the GAFF force field⁷³, with bonded parameters for Zn²⁺ obtained from reported work^{74,75}. RESP2(0.5) partial charges are used for the species involved in this study, which are derived with the help of Multiwfn program by first optimizing the molecular geometry at the B3LYP/TZVP level of theory in Gaussian 16, and then fitting to electrostatic potential calculated at the B3LYP/ma-TZVP level of theory^{76,77}. Van der Waals interactions are described by the Lennard Jones (LJ) potential with a cutoff of 1.2 nm. The LJ parameters between different atom pairs are generated by Lorentz-Berthelot mixing rules. Electrostatic interactions are calculated with the particle-mesh Ewald method with a grid spacing of

0.12 nm and a pme-order of 4. 20-ns production runs are carried out at the same PT condition maintained by Nose-Hoover thermostat and Parrinello-Rahman barostat at $T = 293.15$ K and $P = 1$ bar. The leap-frog algorithm with a time step of 1 fs is used to integrate the equations of motion. Three-dimensional periodic boundary conditions are applied during simulations.

Data availability

The data that support the findings of this study are available within the article and its Supplementary Information files or from the corresponding author upon reasonable request. Source data are provided with this paper.

References

- Zhou, J. et al. Leveling the Zn anode by crystallographic orientation manipulation. *Nano Lett.* **23**, 10148–10156 (2023).
- Dong, D., Wang, T., Sun, Y., Fan, J. & Lu, Y. Hydrotropic solubilization of zinc acetates for sustainable aqueous battery electrolytes. *Nat. Sustain.* **6**, 1474–1484 (2023).
- Zhang, C. et al. The electrolyte comprising more robust water and superhalides transforms Zn-metal anode reversibly and dendrite-free. *Carbon Energy* **3**, 339–348 (2020).
- Zhang, Q. et al. Modulating electrolyte structure for ultralow temperature aqueous zinc batteries. *Nat. Commun.* **11**, 4463 (2020).
- Efaw, C. M. et al. Localized high-concentration electrolytes get more localized through micelle-like structures. *Nat. Mater.* **22**, 1531–1539 (2023).
- Rui, X. et al. In situ polymerization facilitating practical high-safety quasi-solid-state batteries. *Adv. Mater.* **36**, e2402401 (2024).
- Liu, J. et al. Water-tolerant solid polymer electrolyte with high ion-conductivity for simplified battery manufacturing in air surroundings. *Appl. Phys. Lett.* **121**, 153905 (2022).
- Kim, M. S. et al. Suspension electrolyte with modified Li^+ solvation environment for lithium metal batteries. *Nat. Mater.* **21**, 445–454 (2022).
- Hao, J. et al. Low-cost and non-flammable eutectic electrolytes for advanced Zn- I_2 batteries. *Angew. Chem. Int. Ed.* **62**, e202310284 (2023).
- Peng, H. et al. Solvation modulation and reversible SiO_2 -enriched interphase enabled by deep eutectic sol electrolytes for low-temperature zinc metal batteries. *Adv. Energy Mater.* **14**, 2303411 (2024).
- Zhao, M. et al. Semi-immobilized ionic liquid regulator with fast kinetics toward highly stable zinc anode under -35 to 60°C . *Adv. Mater.* **34**, e2203153 (2022).
- Gao, J., Xie, X., Liang, S., Lu, B. & Zhou, J. Inorganic colloidal electrolyte for highly robust zinc-ion batteries. *Nano-micro Lett.* **13**, 69 (2021).
- Guo, H. et al. Stable colloid-in-acid electrolytes for long life proton batteries. *Nano Energy* **102**, 107642 (2022).
- Wang, X. et al. Colloid electrolyte with changed Li^+ solvation structure for high-power, low-temperature lithium-ion batteries. *Adv. Mater.* **35**, 2209140 (2023).
- Zhang, W. et al. A microscopically heterogeneous colloid electrolyte of covalent organic nanosheets for ultrahigh-voltage and low-temperature lithium metal batteries. *Energy Environ. Sci.* **17**, 2642–2650 (2024).
- Cao, J. et al. Regulating solvation structure to stabilize zinc anode by fastening the free water molecules with an inorganic colloidal electrolyte. *Nano Energy* **93**, 106839 (2022).
- Kato, Y. et al. Communication-enhancement of structural stability of $\text{LiNi}_{0.5}\text{Co}_{0.2}\text{Mn}_{0.3}\text{O}_2$ cathode particles against high-voltage cycling by lithium silicate addition. *J. Electrochem. Soc.* **166**, A941–A943 (2019).
- Nian, Q. et al. Regulating frozen electrolyte structure with colloidal dispersion for low temperature aqueous batteries. *Angew. Chem. Int. Ed.* **62**, e202217671 (2023).
- Trefalt, G., Palberg, T. & Borkovec, M. Forces between colloidal particles in aqueous solutions containing monovalent and multivalent ions. *Curr. Opin. Colloid Interface Sci.* **27**, 9–17 (2017).
- Matijević, E. Colloid stability and complex chemistry. *J. Phys. Chem.* **42**, 982 (1938).
- Zhou, J. et al. Diminishing interfacial turbulence by colloid-polymer electrolyte to stabilize zinc ion flux for deep-cycling Zn metal batteries. *Adv. Mater.* **34**, e2200131 (2022).
- Qian, L. et al. Ultralow-salt-concentration electrolyte for high-voltage aqueous Zn metal batteries. *Adv. Funct. Mater.* **33**, 2301118 (2023).
- Yang, M. et al. The construction of anion-induced solvation structures in low-concentration electrolyte for stable zinc anodes. *Angew. Chem. Int. Ed.* **63**, e202400337 (2024).
- Ma, G. et al. Non-flammable, dilute, and hydrous organic electrolytes for reversible Zn batteries. *Chem. Sci.* **13**, 11320–11329 (2022).
- Gourley, S. W. D., Brown, R., Adams, B. D. & Higgins, D. Zinc-ion batteries for stationary energy storage. *Joule* **7**, 1415–1436 (2023).
- Hao, B. et al. Trapping high-activity water in nature-inspired plant-derived separator to realize ultrastable interfacial chemistry of Zn anode. *J. Phys. Chem. Lett.* **14**, 9986–9995 (2023).
- Blanc, L. E., Kundu, D. & Nazar, L. F. Scientific challenges for the implementation of Zn-ion batteries. *Joule* **4**, 771–799 (2020).
- Han, D. et al. A non-flammable hydrous organic electrolyte for sustainable zinc batteries. *Nat. Sustain.* **5**, 205–213 (2021).
- Du, H., Qi, X., Qie, L. & Huang, Y. A nonflammable organic electrolyte with a weak association state for zinc batteries operated at -78.5°C . *Adv. Funct. Mater.* **33**, 2302546 (2023).
- Lv, Y., Xiao, Y., Ma, L., Zhi, C. & Chen, S. Recent advances in electrolytes for “beyond aqueous” zinc-ion batteries. *Adv. Mater.* **34**, 2106409 (2022).
- Chang, N. et al. An aqueous hybrid electrolyte for low-temperature zinc-based energy storage devices. *Energy Environ. Sci.* **13**, 3527–3535 (2020).
- Zhao, Z. et al. Revealing the missing puzzle piece of concentration in regulating Zn electrodeposition. *Proc. Natl. Acad. Sci. USA* **120**, e2307847120 (2023).
- Cheng, Q. et al. Stabilizing lithium plating in polymer electrolytes by concentration-polarization-induced phase transformation. *Joule* **6**, 2372–2389 (2022).
- Brunel, F., Pochard, I., Gauffinet, S., Turesson, M. & Labbez, C. Structure and yielding of colloidal silica gels varying the range of interparticle interactions. *J. Phys. Chem. B* **120**, 5777–5785 (2016).
- Hoffman, Z. J., Galluzzo, M. D., Gordon, M. P., Urban, J. J. & Balsara, N. P. Comparing theoretical salt concentration profiles in a polymer electrolyte with experimental measurements using Operando Raman Spectroscopy. *J. Electrochem. Soc.* **170**, 090517 (2023).
- Rey, I., Bruneel, J. L., Grondin, J., Servant, L. & Lassègues, J. C. Raman spectroelectrochemistry of a lithium/polymer electrolyte symmetric cell. *J. Electrochem. Soc.* **145**, 3034 (1998).
- HIBBEN, J. H. An investigation of intermediate compound formation by means of the Raman Effect. *Proc. Natl. Acad. Sci. USA* **18**, 532–532 (1932).
- Irish, D. E., McCarroll, B. & Young, T. F. Raman study of zinc chloride solutions. *J. Chem. Phys.* **39**, 3436–3444 (1963).
- Kanno, H. & Yamauchi, S. Raman spectral changes of alcoholic zinc chloride solutions from liquid state to glassy state. *J. Solut. Chem.* **20**, 589–594 (1991).
- Dou, H. et al. Steric-hindrance effect tuned ion solvation enabling high performance aqueous zinc ion batteries. *Angew. Chem. Int. Ed.* **63**, e202401974 (2024).

41. Balmer, J. A. et al. Unexpected facile redistribution of adsorbed silica nanoparticles between latexes. *J. Am. Chem. Soc.* **132**, 2166–2168 (2010).
42. Balmer, J. A. et al. Time-resolved small-angle X-ray scattering studies of polymer-silica nanocomposite particles: initial formation and subsequent silica redistribution. *J. Am. Chem. Soc.* **133**, 826–837 (2011).
43. Li, M. et al. Unlocking high-performance organic cathodes: tailoring active group densities in covalent frameworks for aqueous zinc ion batteries. *Energy Mater. Devices* **1**, 9370007 (2023).
44. Yan, T. et al. Refining the inner Helmholtz plane adsorption for achieving a stable solid-electrolyte interphase in reversible aqueous Zn-ion pouch cells. *Energy Storage Mater.* **65**, 103190 (2024).
45. Bendadesse, E. et al. Deciphering the double-layer structure and dynamics on a model Li_xMoO_3 interface by advanced electrogravimetric analysis. *ACS Nano* **16**, 14907–14917 (2022).
46. Qiu, M. et al. Tailoring water structure with high-tetrahedral-entropy for antifreezing electrolytes and energy storage at -80°C . *Nat. Commun.* **14**, 601 (2023).
47. Li, W. et al. Designing ternary hydrated eutectic electrolyte capable of four-electron conversion for advanced Zn- I_2 full batteries. *Energy Environ. Sci.* **16**, 4502–4510 (2023).
48. Li, G. et al. A biocompatible electrolyte enables highly reversible Zn anode for zinc ion battery. *Nat. Commun.* **14**, 6526 (2023).
49. Jin, H. et al. Strong graphene 3D assemblies with high elastic recovery and hardness. *Adv. Mater.* **30**, 1707424 (2018).
50. Pathak, R. et al. Ultrathin bilayer of graphite/ SiO_2 as solid interface for reviving Li metal anode. *Adv. Energy Mater.* **9**, 1901486 (2019).
51. Chen, S., Li, K., Hui, K. S. & Zhang, J. Regulation of lamellar structure of vanadium oxide via polyaniline intercalation for high-performance aqueous zinc-ion battery. *Adv. Funct. Mater.* **30**, 2003890 (2020).
52. Li, R. et al. Intercalated polyaniline in V_2O_5 as a unique vanadium oxide bronze cathode for highly stable aqueous zinc ion battery. *Energy Storage Mater.* **38**, 590–598 (2021).
53. Dou, X., Xie, X., Liang, S. & Fang, G. Low-current-density stability of vanadium-based cathodes for aqueous zinc-ion batteries. *Sci. Bull.* **69**, 833–845 (2024).
54. Xing, Z. et al. Facing the capacity fading of vanadium-based zinc-ion batteries. *Trends Chem.* **5**, 380–392 (2023).
55. Guo, S. et al. Cathode interfacial layer formation via in situ electrochemically charging in aqueous zinc-ion battery. *ACS Nano* **13**, 13456–13464 (2019).
56. Liu, S. et al. Tuning the kinetics of zinc-ion insertion/extraction in V_2O_5 by in situ polyaniline intercalation enables improved aqueous zinc-ion storage performance. *Adv. Mater.* **32**, 2001113 (2020).
57. Li, W. et al. Electron delocalization and dissolution-restraint in vanadium oxide superlattices to boost electrochemical performance of aqueous zinc-ion batteries. *Adv. Energy Mater.* **10**, 2001852 (2020).
58. Ayad, M. M., Rehab, A. F., El-Hallag, I. S. & Amer, W. A. Preparation and characterization of polyaniline films in the presence of N-phenyl-1,4-phenylenediamine. *Eur. Polym. J.* **43**, 2540–2549 (2007).
59. Stejskal, J. & Trchová, M. Aniline oligomers versus polyaniline. *Polym. Int.* **61**, 240–251 (2011).
60. Wang, W. et al. Regulating interfacial reaction through electrolyte chemistry enables gradient interphase for low-temperature zinc metal batteries. *Nat. Commun.* **14**, 5443 (2023).
61. Li, C., Jin, S., Archer, L. A. & Nazar, L. F. Toward practical aqueous zinc-ion batteries for electrochemical energy storage. *Joule* **6**, 1733–1738 (2022).
62. Zampardi, G. & Mantia, L. F. Open challenges and good experimental practices in the research field of aqueous Zn-ion batteries. *Nat. Commun.* **13**, 687 (2022).
63. Wang, Y., Li, Z., Li, X., Ma, Z. & Li, L. Catalyzing battery materials research via lab-made, sub-ampere-hour-scale pouch cells, and long-term electrochemical monitoring by a reparable reference electrode. *Adv. Energy Mater.* **14**, 2304512 (2024).
64. Ji, X. & Nazar, L. F. Best practices for zinc metal batteries. *Nat. Sustain.* **7**, 98–99 (2024).
65. Frenck, L., Sethi, G. K., Maslyn, J. A. & Balsara, N. P. Factors that control the formation of dendrites and other morphologies on lithium metal anodes. *Front. Energy Res.* **7**, 115 (2019).
66. Galluzzo, M. D., Maslyn, J. A., Shah, D. B. & Balsara, N. P. Ohm's law for ion conduction in lithium and beyond-lithium battery electrolytes. *J. Chem. Phys.* **151**, 020901 (2019).
67. Shah, D. B. et al. Effect of anion size on conductivity and transference number of perfluoroether electrolytes with lithium salts. *J. Electrochem. Soc.* **164**, A3511–A3517 (2017).
68. Shah, D. B. et al. Difference between approximate and rigorously measured transference numbers in fluorinated electrolytes. *Phys. Chem. Chem. Phys.* **21**, 7857–7866 (2019).
69. Choo, Y. et al. Complete electrochemical characterization and limiting current of polyacetal electrolytes. *J. Electrochem. Soc.* **169**, 020538 (2022).
70. Fang, C., Yu, X., Chakraborty, S., Balsara, N. P. & Wang, R. Molecular origin of high cation transference in mixtures of poly(pentyl malonate) and lithium salt. *ACS Macro Lett.* **12**, 612–618 (2023).
71. Abraham, M. J. et al. GROMACS: High performance molecular simulations through multi-level parallelism from laptops to supercomputers. *SoftwareX* **1–2**, 19–25 (2015).
72. Allouche, A. R. Gabedit-a graphical user interface for computational chemistry softwares. *J. Comput. Chem.* **32**, 174–182 (2011).
73. Wang, J., Wolf, R. M., Caldwell, J. W., Kollman, P. A. & Case, D. A. Development and testing of a general amber force field. *J. Comput. Chem.* **25**, 1157–1174 (2004).
74. Li, P., Roberts, B. P., Chakravorty, D. K. & Merz, K. M. Rational design of particle Mesh Ewald compatible Lennard-Jones parameters for +2 metal cations in explicit solvent. *J. Chem. Theory Comput.* **9**, 2733–2748 (2013).
75. Li, P. & Merz, K. M. Taking into account the ion-induced dipole interaction in the nonbonded model of ions. *J. Chem. Theory Comput.* **10**, 289–297 (2014).
76. Lu, T. & Chen, F. Multiwfn: a multifunctional wavefunction analyzer. *J. Comput. Chem.* **33**, 580–592 (2012).
77. Schauerl, M. et al. Non-bonded force field model with advanced restrained electrostatic potential charges (RESP2). *Commun. Chem.* **3**, 44 (2020).

Acknowledgements

This research was financially supported by the National Natural Science Foundations of China (Grant Nos. 52302270, 52071226, U21A20332) awarded to J.Z., T.Q. and C.Y., the Natural Science Foundations of Jiangsu Province (Grant No. BK20220061) awarded to T.Q., the Post-graduate Research & Practice Innovation Program of Jiangsu Province (SJCX24_1994) awarded to B.H., the Large Instruments Open Foundation of Nantong University awarded to J.Z., and National-Level Innovative Training Program for College Students of Nantong University awarded to H.Y.

Author contributions

B.H. and J.Z. conceived the idea and designed the experiments. B.H. prepared materials, performed measurements, analyzed the data. H.Y., C.Z., Z.W., and J.L. helped with part of the experiment and data analysis. C.Y. and T.Q. supervised this project. B.H. wrote the draft, J.Z. finalized the manuscript. All authors discussed the results and commented on the manuscript.

Competing interests

The authors declare no competing interests.

Additional information

Supplementary information The online version contains supplementary material available at <https://doi.org/10.1038/s41467-024-53885-z>.

Correspondence and requests for materials should be addressed to Jinqiu Zhou or Tao Qian.

Peer review information *Nature Communications* thanks Minjoon Park and the other, anonymous, reviewer(s) for their contribution to the peer review of this work. A peer review file is available.

Reprints and permissions information is available at <http://www.nature.com/reprints>

Publisher's note Springer Nature remains neutral with regard to jurisdictional claims in published maps and institutional affiliations.

Open Access This article is licensed under a Creative Commons Attribution-NonCommercial-NoDerivatives 4.0 International License, which permits any non-commercial use, sharing, distribution and reproduction in any medium or format, as long as you give appropriate credit to the original author(s) and the source, provide a link to the Creative Commons licence, and indicate if you modified the licensed material. You do not have permission under this licence to share adapted material derived from this article or parts of it. The images or other third party material in this article are included in the article's Creative Commons licence, unless indicated otherwise in a credit line to the material. If material is not included in the article's Creative Commons licence and your intended use is not permitted by statutory regulation or exceeds the permitted use, you will need to obtain permission directly from the copyright holder. To view a copy of this licence, visit <http://creativecommons.org/licenses/by-nc-nd/4.0/>.

© The Author(s) 2024